The Astrophysical Journal Supplement Series, 192:19 (21pp), 2011 February doi:10.1088/0067-0049/192/2/19

SEVEN-YEAR *WILKINSON MICROWAVE ANISOTROPY PROBE* (*WMAP**) OBSERVATIONS: PLANETS AND CELESTIAL CALIBRATION SOURCES

J. L. Weiland[1], N. Odegard[1], R. S. Hill[1], E. Wollack[2], G. Hinshaw[2], M. R. Greason[1], N. Jarosik[3], L. Page[3], C. L. Bennett[4], J. Dunkley[5], B. Gold[4], M. Halpern[6], A. Kogut[2], E. Komatsu[7], D. Larson[4], M. Limon[8], S. S. Meyer[9], M. R. Nolta[10], K. M. Smith[11], D. N. Spergel[11,12], G. S. Tucker[13], and E. L. Wright[14]

[1] ADNET Systems, Inc., 7515 Mission Dr., Suite A100 Lanham, MD 20706, USA; jweiland@sesda2.com
[2] Code 665, NASA/Goddard Space Flight Center, Greenbelt, MD 20771, USA
[3] Department of Physics, Jadwin Hall, Princeton University, Princeton, NJ 08544-0708, USA
[4] Department of Physics and Astronomy, The Johns Hopkins University, 3400 N. Charles St., Baltimore, MD 21218-2686, USA
[5] Astrophysics, University of Oxford, Keble Road, Oxford, OX1 3RH, UK
[6] Department of Physics and Astronomy, University of British Columbia, Vancouver, BC V6T 1Z1, Canada
[7] Department of Astronomy, University of Texas, 2511 Speedway, RLM 15.306, Austin, TX 78712, USA
[8] Columbia Astrophysics Laboratory, 550 W. 120th St., Mail Code 5247, New York, NY 10027-6902, USA
[9] Departments of Astrophysics and Physics, KICP and EFI, University of Chicago, Chicago, IL 60637, USA
[10] Canadian Institute for Theoretical Astrophysics, 60 St. George St, University of Toronto, Toronto, ON M5S 3H8, Canada
[11] Department of Astrophysical Sciences, Peyton Hall, Princeton University, Princeton, NJ 08544-1001, USA
[12] Princeton Center for Theoretical Physics, Princeton University, Princeton, NJ 08544, USA
[13] Department of Physics, Brown University, 182 Hope St., Providence, RI 02912-1843, USA
[14] UCLA Physics and Astronomy, P.O. Box 951547, Los Angeles, CA 90095–1547, USA
Received 2010 January 26; accepted 2010 June 7; published 2011 January 11

ABSTRACT

We present *WMAP* seven-year observations of bright sources which are often used as calibrators at microwave frequencies. Ten objects are studied in five frequency bands (23–94 GHz): the outer planets (Mars, Jupiter, Saturn, Uranus, and Neptune) and five fixed celestial sources (Cas A, Tau A, Cyg A, 3C274, and 3C58). The seven-year analysis of Jupiter provides temperatures which are within 1σ of the previously published *WMAP* five-year values, with slightly tighter constraints on variability with orbital phase ($0.2\% \pm 0.4\%$), and limits (but no detections) on linear polarization. Observed temperatures for both Mars and Saturn vary significantly with viewing geometry. Scaling factors are provided which, when multiplied by the Wright Mars thermal model predictions at 350 μm, reproduce *WMAP* seasonally averaged observations of Mars within $\sim 2\%$. An empirical model is described which fits brightness variations of Saturn due to geometrical effects and can be used to predict the *WMAP* observations to within 3%. Seven-year mean temperatures for Uranus and Neptune are also tabulated. Uncertainties in Uranus temperatures are 3%–4% in the 41, 61, and 94 GHz bands; the smallest uncertainty for Neptune is 8% for the 94 GHz band. Intriguingly, the spectrum of Uranus appears to show a dip at ~30 GHz of unidentified origin, although the feature is not of high statistical significance. Flux densities for the five selected fixed celestial sources are derived from the seven-year *WMAP* sky maps and are tabulated for Stokes *I*, *Q*, and *U*, along with polarization fraction and position angle. Fractional uncertainties for the Stokes *I* fluxes are typically 1% to 3%. Source variability over the seven-year baseline is also estimated. Significant secular decrease is seen for Cas A and Tau A: our results are consistent with a frequency-independent decrease of about 0.53% per year for Cas A and 0.22% per year for Tau A. We present *WMAP* polarization data with uncertainties of a few percent for Tau A. Where appropriate, *WMAP* results are compared against previous findings in the literature. With an absolute calibration uncertainty of 0.2%, *WMAP* data are a valuable asset for calibration work.

Key words: galaxies: individual (Cygnus A, 3C274) – ISM: supernova remnants – planets and satellites: general – radio continuum: general – space vehicles: instruments

1. INTRODUCTION

The primary goal of the *Wilkinson Microwave Anisotropy Probe* (*WMAP*) mission (Bennett et al. 2003b) is to study the cosmic microwave background (CMB) anisotropy, an undertaking that requires detailed knowledge of the instrumental angular response and noise, low systematic errors, and absolute calibration at sub-percent levels. These attributes make *WMAP* data of natural interest for ancillary studies of sky-based calibration objects. This paper focuses on *WMAP* observations of selected planets and fixed celestial objects which have been commonly used as calibrators in the microwave, either by ground- or space-based instruments. We provide fundamental measurements for these objects which will be of use not only for calibration purposes, but also other studies, such as planetary radiative transfer.

A brief discussion of *WMAP* planetary radiometric data was made by Hill et al. (2009), with an earlier discussion of Jupiter temperatures by Page et al. (2003b). We extend these presentations to include *WMAP* observations of Mars, Jupiter, Saturn, Uranus, and Neptune over a seven-year interval (2001–2008), in five microwave passbands ranging from ~23 to 94 GHz. We also select five bright celestial sources for more detailed study: Cas A, Cyg A, Tau A, 3C58, and 3C274. The *WMAP* project routinely compiles and distributes a point-source catalog, which tabulates mean flux values in those same five passbands for bright sources off the Galactic plane (Wright et al. 2009; Hinshaw et al. 2007; Bennett et al. 2003a). However,

* *WMAP* is the result of a partnership between Princeton University and NASA's Goddard Space Flight Center. Scientific guidance is provided by the *WMAP* Science Team.

four of the five objects discussed here (Cas A, Tau A, Cyg A, 3C 58) have low Galactic latitudes and are not included in the catalog. An earlier analysis of three-year *WMAP* Tau A observations by Page et al. (2007) included both intensity and linear polarization measurements.

This paper is one of a suite that details the analysis of *WMAP* seven-year data. An overview and description of data processing methods is provided by Jarosik et al. (2011). Gold et al. (2011) discuss Galactic foregrounds and techniques for removing them; an updated point-source catalog is included. Analysis of CMB power spectra, best-fit models, and cosmological interpretations are presented by Larson et al. (2011) and Komatsu et al. (2011). Bennett et al. (2011) assess potential CMB "anomalies" relative to the best-fit six parameter ΛCDM model.

We organize this paper as follows: a short discussion of the *WMAP* instrument, plus data strengths and limitations for calibration source work, is provided in Section 2. The paper then divides into two major sections: analysis and results for planets (Section 3), and then Section 4 discusses analysis methods and results for the five bright celestial sources. A closing summary and conclusions follow in Section 5.

2. *WMAP* OVERVIEW

Since its arrival at the Earth–Sun L2 point in 2001 August, *WMAP* has produced a well-calibrated, multi-wavelength microwave survey of the entire sky with high-sampling redundancy. Detailed descriptions of the mission profile and hardware can be found in Bennett et al. (2003b), Jarosik et al. (2003a), and Page et al. (2003b). To assist with clarifying the terminology and analysis methods presented in this paper, we describe the key features of the mission.

WMAP observes the sky differentially: signal from the sky is simultaneously sampled in two different directions $\sim 140^\circ$ apart and guided by 10 feed horn pairs into 10 receivers, referred to as differencing assemblies (DAs). The receivers cover five frequency bands (K, Ka, Q, V, and W) with approximate center frequencies of ∼23, 33, 41, 61, and 94 GHz, respectively. There is one DA each for K and Ka bands (K1, Ka1), two DAs each for Q and V bands (Q1, Q2, V1, V2) and four DAs (W1, W2, W3, W4) for W band. The frequency passbands are broad (∼ 20% fractional bandwidth), so that the exact frequency associated with an observation depends on the source spectrum. An orthomode transducer at the throat of each feed separates the sky signal into two orthogonal polarizations, allowing for reconstruction of both intensity and linear polarization signals. Angular resolution is moderate, ranging from roughly $0.^\circ 2$ FWHM in the W band to $\sim 0.^\circ 9$ FWHM in K band.

As a survey mission, *WMAP* is not commanded to point at specific targets, but executes a pole-to-pole sky-scanning strategy whose position on the ecliptic advances $\sim 1^\circ$ each day. To facilitate high redundancy in sky coverage, the spacecraft rotates about a spin axis, which also precesses. These combined motions produce a $\sim 45^\circ$ wide scan swath which looks like a "belt" projected onto the sky, passing through the ecliptic poles. The scan swath returns to its original starting position on the ecliptic every year, after completing a full-sky survey with multiple observations per sky pixel.

A primary strength of *WMAP* data is the calibration accuracy, with an absolute calibration error of 0.2% (Jarosik et al. 2011). The absolute calibration is tied to knowledge of the CMB monopole and the spacecraft orbital velocity, and thus is independent of any reliance on previously established measurements of the sources under study. When coupled with *WMAP*'s temporal and spectral coverage, the accurate flux measurements can provide a useful measure of intrinsic or geometrically induced source variability.

There are some limiting factors, however. Temporal coverage of an object is constrained by the sky-scanning method. For a fixed source on the ecliptic, the *WMAP* scan strategy provides for two ∼45 day windows a year in which to observe that source. These "observing seasons" are spaced roughly six months apart. While this geometry is modified somewhat for moving objects, only Mars is near enough that the orbital motion can extend a single viewing window from 45 days to as much as 60 to 90 days. Since *WMAP* does not dwell on an object, but simply scans as it passes through the viewing swath, the number of observations for an individual object is also limited, which affects the signal-to-noise. Finally, *WMAP*'s moderate spatial resolution, which allows us to characterize the planets as calibrators, also places detailed knowledge of structures such as Saturn's rings beyond instrument capabilities.

3. PLANETS

There are five planets with sufficient signal-to-noise for analysis. Listed in order of decreasing signal-to-noise, these are Jupiter, Saturn, Mars, Uranus, and Neptune. Since *WMAP* points away from the Sun, Earth, and Moon in its L2 orbit, it cannot observe Mercury or Venus.

3.1. Data Processing and Analysis Methods

Planets are excluded from the standard map-based products used for *WMAP* studies of the CMB and Galactic foregrounds. Observations of the planets must be extracted from the calibrated time-ordered data (TOD), and then undergo quality assessment and background removal before they can be analyzed. The extraction process gathers all observations from the TOD taken within several degrees of each planet and associates ancillary information such as position in the focal plane, attitude, planet-viewing aspect, and data quality flags with each observation. Observations whose sky positions lie within 7° radius of other planets or which are of suspect quality are immediately rejected. In addition, observations are excluded from use if either beam of a DA feed-horn pair samples sky coordinates that fall within the boundaries of a spatial processing mask (Jarosik et al. 2007). The purpose of this "Galactic masking" is to mitigate background removal error by excluding observations located near strong-signal, high-gradient regions of the Galaxy. For those observations which survive these quality control steps, Galactic and CMB background signals are subtracted. The background signal subtracted from each observation is computed from the DA-appropriate seven-year mean map (from which planetary data were excluded), using the value from the $\sim 6'$ wide pixel which is closest in spatial coordinates to those of the time-ordered observation. Table 1 lists the beginning and ending dates of the observing seasons for the five planets, i.e., when they are directly in the *WMAP* viewing swath. The "sky proximity" column in the table indicate probable reasons for an unusually high rejection of observations within a season.

As noted in Page et al. (2003b), planets are "point sources" for *WMAP* and thus the brightness temperature of a planet T_p can be computed via the relation

$$T_p \Omega_p = T^m \Omega_B, \quad (1)$$

where T^m is the peak response observed by *WMAP*, Ω_B is the main-beam solid angle, and Ω_p is the solid angle subtended by

Table 1
WMAP Planet Observing Seasons (2001–2008)

Planet	Season[a]	Begin	End	SP[b]
Jupiter	1	2001 Oct 8	2001 Nov 22	
	2	2002 Feb 11	2002 Mar 27	G
	3	2002 Nov 10	2002 Dec 24	
	4	2003 Mar 15	2003 Apr 29	G
	5	2003 Dec 11	2004 Jan 23	
	6	2004 Apr 15	2004 May 30	
	7	2005 Jan 9	2005 Feb 21	
	8	2005 May 16	2005 Jul 1	
	9	2006 Feb 7	2006 Mar 24	
	10	2006 Jun 16	2006 Aug 2	
	11	2007 Mar 10	2007 Apr 24	
	12	2007 Jul 19	2007 Sep 3	
	13	2008 Apr 11	2008 May 27	
Saturn	1	2001 Sep 7	2001 Oct 22	
	2	2002 Jan 14	2002 Feb 26	
	3	2002 Sep 22	2002 Nov 5	
	4	2003 Jan 28	2003 Mar 13	G
	5	2003 Oct 7	2003 Nov 20	
	6	2004 Feb 12	2004 Mar 26	G
	7	2004 Oct 20	2004 Dec 3	
	8	2005 Feb 25	2005 Apr 10	
	9	2005 Nov 4	2005 Dec 17	
	10	2006 Mar 11	2006 Apr 24	
	11	2006 Nov 18	2006 Dec 31	
	12	2007 Mar 25	2007 May 9	
	13	2007 Dec 1	2008 Jan 13	
	14	2008 Apr 7	2008 May 22	
Mars	1	2001 Aug 10	2001 Oct 14	
	2	2003 Apr 19	2003 Jul 17	U, N
	3	2003 Oct 10	2003 Dec 30	U
	4	2005 Jul 13	2005 Oct 1	
	5	2005 Dec 16	2006 Feb 19	
	6	2007 Sep 18	2007 Nov 20	
	7	2008 Jan 30	2008 Mar 30	
Uranus	1	2001 Sep 30	2001 Nov 13	
	2	2002 May 20	2002 Jul 5	
	3	2002 Oct 4	2002 Nov 17	
	4	2003 May 25	2003 Jul 9	M
	5	2003 Oct 8	2003 Nov 21	M
	6	2004 May 28	2004 Jul 13	
	7	2004 Oct 12	2004 Nov 24	
	8	2005 Jun 2	2005 Jul 17	
	9	2005 Oct 16	2005 Nov 28	
	10	2006 Jun 6	2006 Jul 22	
	11	2006 Oct 20	2006 Dec 3	
	12	2007 Jun 10	2007 Jul 26	
	13	2007 Oct 24	2007 Dec 7	
	14	2008 Jun 14	2008 Jul 29	
Neptune	1	2001 Sep 15	2001 Oct 29	
	2	2002 May 2	2002 Jun 16	
	3	2002 Sep 17	2002 Oct 31	
	4	2003 May 4	2003 Jun 19	M
	5	2003 Sep 20	2003 Nov 3	
	6	2004 May 6	2004 Jun 21	
	7	2004 Sep 21	2004 Nov 4	
	8	2005 May 8	2005 Jun 23	
	9	2005 Sep 23	2005 Nov 7	
	10	2006 May 11	2006 Jun 26	
	11	2006 Sep 26	2006 Nov 9	
	12	2007 May 14	2007 Jun 28	
	13	2007 Sep 28	2007 Nov 11	
	14	2008 May 15	2008 Jun 30	

Notes.
[a] An observing season is defined as a contiguous time interval during which an object is in the *WMAP* viewing swath.
[b] sky coordinate proximity to any of the following: Galactic plane (G); Mars (M), Uranus (U), Neptune (N).

Table 2
Adopted Planetary Radii[a] and fiducial Solid Angles

Planet	$R_{\rm eq}$ (km)	$R_{\rm pole}$ (km)	$\Omega_{\rm ref}$[b] (sr)
Mars	3396	3376	7.153×10^{-10}
Jupiter	71492	66854	2.481×10^{-8}
Saturn	60268	54364	5.096×10^{-9}
Uranus	25559	24973	2.482×10^{-10}
Neptune	24764	24341	1.006×10^{-10}

Notes.
[a] From Seidelmann et al. (2007).
[b] Solid angle computed at fiducial distances of 1.5, 5.2, 9.5, 19, and 29 AU, respectively. See Section 3.1 for further discussion.

the planet. Changing distance between the planet and *WMAP*, plus changes in viewing aspect of an oblate planet, will cause Ω_p (and also T^m) to vary with time. We account for both geometrical effects and compute the brightness temperature relative to a fiducial solid angle $\Omega_p^{\rm ref}$ via the use of time-dependent geometrical scaling factors f_d and f_A. The factors f_d and f_A may be thought of as "distance correction" and "disk oblateness correction" factors

$$T_p = T^m \Omega_B / \Omega_p^{\rm ref} \times f_d / f_A \quad (2)$$

$$f_A = A_{\rm disk}^{\rm proj} / A_{\rm ref} \quad (3)$$

$$f_d = d_p^2 / d_{\rm ref}^2, \quad (4)$$

where $A_{\rm ref}$ and $d_{\rm ref}$ are a fixed fiducial disk area and distance, respectively. $A_{\rm disk}^{\rm proj}$ is the projected area of the planetary disk, and d_p the distance of the planet from *WMAP*, at the time of each observation. The projected area of the oblate disk is computed from

$$A_{\rm disk}^{\rm proj} = \pi R_{\rm pole}^{\rm proj} R_{\rm eq}, \quad (5)$$

where $R_{\rm eq}$ is the planet's equatorial radius and $R_{\rm pole}^{\rm proj}$ is the projected polar radius given by

$$R_{\rm pole}^{\rm proj} = R_{\rm pole}[1 - \sin^2(D_W)(1 - (R_{\rm pole}/R_{\rm eq})^2)]^{1/2}, \quad (6)$$

where D_W is the planetary latitude of *WMAP* ("sub-*WMAP* latitude"). The fiducial disk area $A_{\rm ref}$ is simply $A_{\rm disk}^{\rm proj}$ evaluated at D_W of 0°. Planetary radii and north pole directions used to compute D_W are adopted from Seidelmann et al. (2007); the polar and equatorial radii are listed in Table 2. Because *WMAP* is at L2, D_W is not very dissimilar to that of the sub-Earth latitude, D_e.

As the brightest "point source" visible to *WMAP*, Jupiter is used to characterize the main beam response of the instrument. This process and analysis are described in detail in Hill et al. (2009), N. Jarosik et al. (2011), and Page et al. (2003b). The end result is a set of seven-year, azimuthally symmetrized, one-dimensional radial beam profiles per DA. These radial beam profiles are then used to derive window functions used for CMB power-spectrum deconvolution. Unlike the rest of the planetary temperatures in this section, the seven-year mean Jupiter temperatures are derived from the $l = 0$ value of the unnormalized window functions (which measures $T^m \Omega_B$), coupled with the fiducial solid angle for Jupiter (Hill et al. 2009). For all other planetary analysis, brightness temperatures are derived using a template-fitting technique, which takes advantage of the high-quality beam information obtained from

seven years of Jupiter observations. After the processing steps described above, radial response profiles are produced for each planet, per DA, per season, by assigning observations to 0.25 arcmin bins increasing in angular distance from the planet's center. Each bin is assigned a mean value and an error based on instrument noise appropriate to the number of observations within the bin. The known radial beam response, based on seven-year Jupiter data, is used as a fitting template to the seasonal radial profile for each DA. The fit returns T^m for the planet. The brightness temperature is then derived from T^m, the main-beam solid angle (Jarosik et al. 2011) and the reference solid angle for the planet as per the above equations. Errors include the formal error in the template coefficient and the propagated error in the beam solid angle. Figure 1 illustrates sample W1 radial profiles for a single observing season for each of the planets. The beam template is overplotted in red. As well as illustrating the technique, the figure is also a useful comparator of signal quality for each planet at the W band. Beam dilution increases with decreasing *WMAP* frequency: Ω_B is roughly 24.6, 14.4, 8.98, 4.20, and 2.10 $\times 10^{-5}$ sr for the K–W bands, respectively (Jarosik et al. 2011).

Tabulated brightness temperatures are appropriate for the Rayleigh–Jeans (RJ) approximation. Brightness temperatures provided in the Tables do not include the CMB contribution blocked by the planet but included in the background. As noted in the Tables, absolute brightness temperature is obtained by adding 2.2, 2.0, 1.9, 1.5, and 1.1 K in bands K, Ka, Q, V, and W, respectively (Page et al. 2003a), since in the RJ approximation the CMB temperatures are frequency dependent. *WMAP* data points shown in comparison to measurements in the literature are converted to absolute brightness.

3.2. Jupiter

Jupiter is a bright, accessible source whose whole-disk observations have long been used for calibration in the infrared through radio. Hill et al. (2009) recommend the use of *WMAP* radiometry of Jupiter as the preferred method of transferring the *WMAP* dipole calibration to another microwave instrument. For some instruments, Jupiter is unfortunately too bright, hence the interest in the use of fainter sources, and a set of observations which tie several common sources together on the same calibration scale. We continue to recommend Jupiter as the primary comparison calibrator, however.

Seven-year mean brightness temperatures for Jupiter, computed as described in Section 3.1, are presented in Table 3. The seven-year values differ from those of the five-year analysis of Hill et al. (2009) by 1σ or less. The largest changes, which hover near 1σ, are for the K band and some of the W-band DAs. A detailed explanation of these changes is given in Jarosik et al. (2011). Briefly, the change in K-band results from improved background subtraction, and the W-band changes are driven by small revisions to the beam solid angles, based on modeling. The seven-year temperatures for the W band show a decreased scatter between the individual DAs compared to five-year, implying an improved calibration. The Jupiter temperature uncertainties listed in Table 3 are derived from the quadrature sum of the solid angle error and absolute calibration error of 0.2% (Jarosik et al. 2011), as they were in the five-year analysis.

Thermal emission from Jupiter's atmosphere is the primary signal source at wavelengths spanned by *WMAP*. As such, the observations are helpful for providing constraints on atmospheric models for Jupiter, which in turn could be used for calibration purposes. However, as noted by e.g., Gibson et al. (2005), there is a fine point to consider: small contributions to

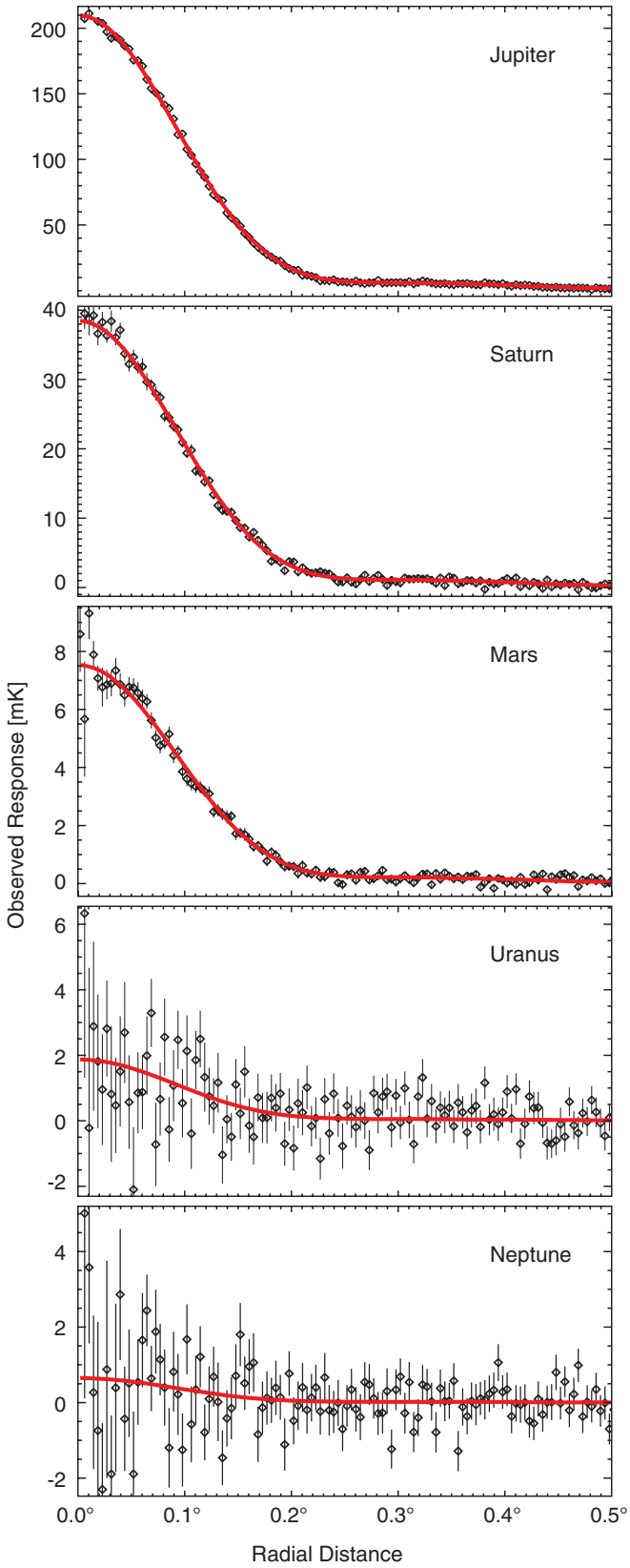

Figure 1. Typical single-season radial profiles of Jupiter, Saturn, Mars, Uranus, and Neptune for the W1 differencing assembly. Black points are data, red line is the fit of the smooth beam profile template from which the temperatures are computed. The signal-to-noise ratio is best for Jupiter and worst for Neptune.

Table 3
Seven-year Mean Jupiter Temperatures

DA/Band	ν_e^{RJ} [a] (GHz)	λ [b] (mm)	T [c] (K)	$\sigma(T)$ [d] (K)
Per DA				
K1	22.85	13.1	136.2	0.85
Ka1	33.11	9.1	147.2	0.77
Q1	40.92	7.3	154.4	0.91
Q2	40.71	7.4	155.2	0.87
V1	60.41	5.0	165.0	0.78
V2	61.28	4.9	166.1	0.74
W1	93.25	3.2	173.0	0.84
W2	93.73	3.2	173.3	0.91
W3	93.72	3.2	173.7	0.94
W4	93.57	3.2	173.9	0.92
Per band				
K	22.85	13.1	136.2	0.85
Ka	33.11	9.1	147.2	0.77
Q	40.82	7.3	154.8	0.67
V	60.85	4.9	165.6	0.59
W	93.32	3.2	173.5	0.54

Notes.
[a] Seven-year values; see Jarosik et al. (2011).
[b] $\lambda = c/\nu_e^{RJ}$.
[c] Brightness temperature calculated for a solid angle $\Omega_{ref} = 2.481 \times 10^{-8}$ sr at a fiducial distance of 5.2 AU. Temperature is with respect to blank sky: absolute brightness temperature is obtained by adding 2.2, 2.0, 1.9, 1.5, and 1.1 K in bands K, Ka, Q, V, and W, respectively (Page et al. 2003a). Jupiter temperatures are uncorrected for a small synchrotron emission component (see Section 3.2).
[d] Computed from errors in Ω_B (Jarosik et al. 2011) summed in quadrature with absolute calibration error of 0.2%.

the total observed intensity from a synchrotron component up to about 40 GHz are expected. This non-thermal "decimetric emission" arises from charged particles trapped close to Jupiter by its strong magnetic field, and dominates the spectrum at frequencies less than about 3 GHz. Estimates in the literature place the synchrotron contribution at 23 GHz near 1% of the total intensity (de Pater & Dunn 2003; Gibson et al. 2005), with a roughly $T \sim \nu^{-2.4}$ frequency dependence (Klein & Gulkis 1978). However, the synchrotron emission is known to be variable on a wide range of timescales (Santos-Costa et al. 2009; de Pater & Dunn 2003; de Pater et al. 2003; Miyoshi et al. 2000), and accurate removal is difficult. The *WMAP* seven-year mean Jupiter brightness temperatures are graphically compared against those in the literature in Figure 2. Ground-based observational values are taken from compilations of Joiner & Steffes (1991) and Klein & Gulkis (1978), along with individual observations from de Pater et al. (1982, 2001), Greve et al. (1994), and Goldin et al. (1997). Estimates of the synchrotron emission have been removed from the observations in the figure by many, but not all, of the authors, and not necessarily to the same level. The *WMAP* observations are plotted "as observed".

As an estimate of the stability of Jupiter's emission with orbital phase over the seven-year interval, we extend the five-year analysis of Hill et al. (2009), in which temperatures for individual Jupiter observing seasons are computed and compared to the multi-year mean values. Individual seasonal temperatures are derived using the same beam-profile fitting technique which is used for the other planets (Section 3.1). We compute $\Delta T/T$ as the mean deviation of all DAs from their seven-year mean values, and include a 1σ standard deviation as a measure of coherency. These results are listed in Table 4.

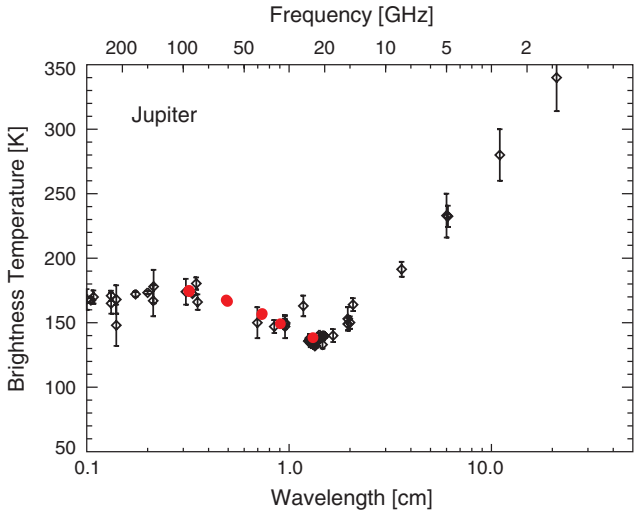

Figure 2. Microwave spectrum of Jupiter. Black diamonds are selected observations compiled from the literature (see the text). The seven-year mean *WMAP* temperatures, corrected to absolute brightness and including error bars, are shown in red. Strong absorption by NH_3 inversion band is centered near 1.3 cm. Minor contributions from synchrotron emission have not been removed from the *WMAP* data (see Section 3.2).

Using the *WMAP* five-year data, Hill et al. (2009) quote an upper limit of $0.3\% \pm 0.5\%$ based on the largest deviation and scatter seen in the first 10 observing seasons, which occurred in season four. A careful examination of the entries in Table 4 with the largest deviations and/or scatter (observing seasons 4, 11, 12) shows that these particular instances have more to do with template fitting and background subtraction quality than with intrinsic source variability. The two seasons with high scatter (4, 12) are those in which the number of available observations for fitting has been significantly reduced because of foreground masking ("% masked" in the Table), which increases the statistical error in the temperature determination. Season 11, with the highest $\Delta T/T$, is one in which Jupiter is nearly aligned with the Galactic center, but outside the processing mask. This is a region in which background subtraction is subject to greater error because of higher temperature gradients across the pixels in the map used for background removal. If one ignores these three entries, then an upper limit of $0.2\% \pm 0.4\%$ is more appropriate. We also searched for indications that the K band might be more intrinsically variable than the W band, because of the small synchrotron contribution. There is no indication of such a frequency dependence in the data, but the upper envelope here is about 0.5%.

The *WMAP* Jupiter observations were analyzed to determine if any linear polarization signal could be detected. A special version of the beam mapping software was run for Jupiter, in which the angle between the polarization axis of each radiometer and the planet's magnetic dipole was computed for each observation. For each differencing assembly, all observations within a tight radius of beam center were accumulated, corrected to peak beam response, background subtracted, loss imbalance corrected, separated by radiometer, and then used to solve for Stokes parameters I, Q, U and their errors. For a more complete description of the relevant equations, see Hinshaw et al. (2003) and Jarosik et al. (2007). Normalized Stokes parameters Q/I and U/I are reported in Table 5, along with their propagated errors and estimated linear polarization fraction, $p_{lin} = \sqrt{(Q/I)^2 + (U/I)^2}$. No attempt has been made to correct for noise bias in either

Table 4
Jupiter Temperature Changes by Season

Season[a]	Start	End	$\Delta T/T$ (%)		% Masked[d]	Mean Position[e]	
			Mean[b]	Scatter[c]		l	b
1	2001 Oct 08	2001 Nov 22	0.11	0.28	0	194	13
2	2002 Feb 11	2002 Mar 27	...	...	95	189	5
3	2002 Nov 10	2002 Dec 24	−0.13	0.28	0	214	40
4	2003 Mar 15	2003 Apr 29	−0.28	0.48	60	206	32
5	2003 Dec 11	2004 Jan 23	0.01	0.22	0	254	59
6	2004 Apr 15	2004 May 30	−0.01	0.32	0	237	55
7	2005 Jan 09	2005 Feb 21	0.00	0.27	12	311	56
8	2005 May 16	2005 Jul 01	−0.08	0.39	0	294	60
9	2006 Feb 07	2006 Mar 24	0.13	0.29	18	344	35
10	2006 Jun 16	2006 Aug 02	0.03	0.45	0	335	43
11	2007 Mar 10	2007 Apr 24	0.41	0.31	0	2	9
12	2007 Jul 19	2007 Sep 03	−0.11	0.49	42	356	17
13	2008 Apr 11	2008 May 27	−0.20	0.37	0	17	−19

Notes.
[a] Season 2 omitted from analysis because Jupiter is aligned with the Galactic plane.
[b] Mean of the percentage temperature change among the DAs for each season, relative to the seven-year mean.
[c] 1σ scatter in the percentage temperature change among the DAs for each season.
[d] Typical percentage of available observations within 0.°5 of planet center which are excluded from analysis because of Galactic plane masking.
[e] Approximate seasonal Jupiter position in Galactic coordinates at mean time of unmasked observations.

Table 5
Jupiter Linear Polarization

DA	Q/I (%)	$\sigma(Q/I)$[a] (%)	U/I (%)	$\sigma(U/I)$[b] (%)	$p_{\rm lin}$[c] (%)	$\sigma(p_{\rm lin})$[d] (%)	S/N[e]
K1	−0.306	0.601	0.658	0.428	0.726	0.464	1.62
Ka1	−0.181	0.408	−0.191	0.293	0.263	0.352	0.79
Q1	−0.168	0.430	−0.244	0.304	0.296	0.349	0.90
Q2	−0.151	0.428	−0.062	0.297	0.163	0.411	0.41
V1	−0.149	0.358	0.462	0.252	0.486	0.263	1.88
V2	0.143	0.305	0.067	0.223	0.158	0.292	0.56
W1	0.040	0.319	0.393	0.233	0.395	0.234	1.69
W2	0.156	0.380	0.188	0.264	0.245	0.317	0.82
W3	0.006	0.397	−0.377	0.277	0.377	0.277	1.36
W4	−0.058	0.371	0.311	0.273	0.316	0.277	1.15

Notes.
[a] Propagated error from σ_I and σ_Q.
[b] Propagated error from σ_I and σ_U.
[c] $p_{\rm lin} = \sqrt{(Q/I)^2 + (U/I)^2}$.
[d] Propagated error.
[e] $\mathrm{S/N} = p_{\rm lin}/\sigma(p_{\rm lin})$.

$p_{\rm lin}$ or its reported error, which is simply the propagated error. The estimated signal-to-noise is low, with no significant detections in any differencing assembly. Linear polarization of the synchrotron emission at 15 and 22 GHz has been detected by de Pater & Dunn (2003) using the Very Large Array (VLA). They were unable to obtain a synchrotron polarization fraction at 22 GHz, but estimated 20% polarization based on the 15 GHz observations, which implies roughly a 0.2% polarization fraction at the K band using a combined thermal and non-thermal intensity. The *WMAP* results are consistent with this estimate, but do not provide any further constraint.

3.3. Mars

Mars' value as a calibrator depends upon the accuracy to which its whole-disk brightness variations (both apparent and intrinsic) can be modeled. Much of the perceived variability from earth-orbit is attributable to geometrical factors: the apparent phase as seen by the observer and changes in solar irradiance as Mars' distance from the Sun varies in its elliptical orbit (Wright 1976). There are a number of additional complexities, however. The day/night cycle imparts a significant rotational modulation to the observed temperature as the surface heats and cools. In the infrared, variable atmospheric effects including molecular line absorption and dust storms can be of importance. Additionally, the Martian surface is itself far from homogenous, with polar ice-caps of changing extent and variations in albedo and thermal inertia on relatively small scales (Putzig & Mellon 2007; Christensen et al. 2001).

Planetary science studies notwithstanding, the astronomical community has most consistently referenced two basic models when calibrating to Mars: the "Wright model" (Wright 1976; Wright & Odenwald 1980; Wright 2007) and the "Rudy model" (Rudy et al. 1987; Muhleman & Berge 1991), both developed before the current level of detail available from orbiters such as Mars Global Surveyor (MGS). In the thermal emission regime ($\lambda \gtrsim 10\ \mu$m), the planet's brightness temperature can be computed to first order as re-emission of absorbed solar energy by a surface layer with a characteristic albedo, emissivity and thermal inertia (de Pater 1990). The Wright model uses this approach to predict thermal emission in the 10–350 μm range, with no positional variations of parameters such as albedo and thermal inertia. The Rudy model originates from VLA observations at 2 and 6 cm, which sample further into the Martian subsurface. Concurrent measurements of the polarized flux are used to estimate radio reflectivities and absorption lengths as a function of planetary latitude, and brightness temperatures calculated via radiative transfer as a function of position on a longitude/latitude grid. Typical errors on T_b quoted for the Wright model are ±5%, or about ±10K, and those for the Rudy model at 5%–10%. We have chosen in this paper to compare the *WMAP* observations against predictions from the Wright model, primarily because of its long history of use and readily available model code (Wright 2007), but also because the seasonal brightness temperatures quoted for *WMAP* are the resultant average over several weeks of data, which means we are only sampling mean properties at best. We have modified the 2007 Wright model code in three ways: (1) JPL ephemeris positions are substituted for the lower precision formulae originally used, (2) an option is added to use *WMAP* spacecraft positions rather than those of the Earth, and (3) computations are extended out to *WMAP* frequencies. The first two changes are not critical to the analysis, as the combined modifications introduce at most at 0.6 K difference from the original results. Typically the model predicts brightness temperatures at 3 mm which are a few Kelvins lower than those at 350 μm, and the temperature spread between the extrema of the 5 *WMAP* frequencies is quite low, of order 0.5 K.

Hill et al. (2009) presented the first five years of *WMAP* Mars observations at 94 GHz. Here we extend the W-band observations to seven years, and include the observations at the other four *WMAP* frequencies. Mean brightness temperatures for Mars at five frequencies and seven *WMAP* observing seasons derived from the seven-year data are presented in Table 6. After correcting to absolute brightness temperature and converting

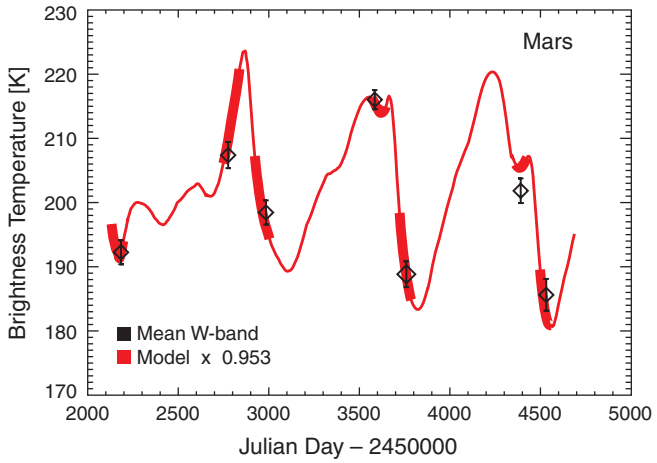

Figure 3. Comparison of *WMAP W*-band seasonal averages (black diamonds; Table 6) to the Mars model of Wright (1976, 2007). The *WMAP* observations have been corrected to absolute brightness. Model values (red line) have been rescaled by a factor of 0.953 to bring them into overall agreement with the observations; thick portions of the line indicate observing seasons. Data quality masking can skew the mean times of observations from the mean of the seasonal interval, as is evident in the second observing season.

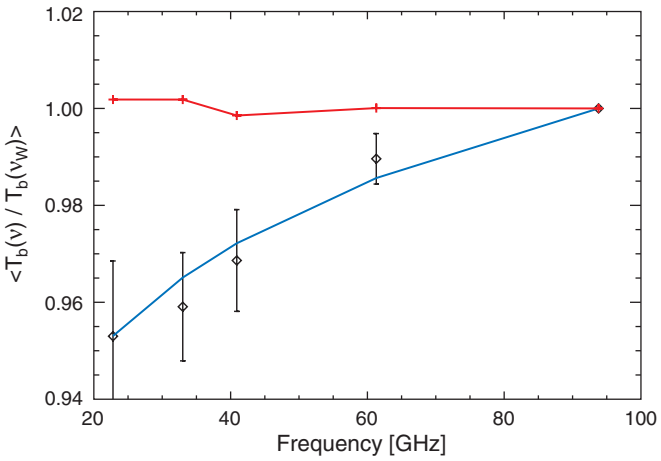

Figure 4. Seven-year mean Mars brightness temperatures as a function of frequency, normalized within each season to T_b at the W band. Black diamonds are the *WMAP* data; error bars are obtained from the variation over the seven observing seasons within each frequency band. The same averaging procedure is carried out using the Wright model predictions for the mean time of observation (red line): small time-sampling and spectral variations between the frequencies cause a slightly jagged appearance. The *WMAP* data show a weak frequency dependence which can be approximated as $(\nu(\mathrm{GHz})/94)^{0.03}$ (blue line). This can be interpreted as a frequency-dependent emissivity.

from Rayleigh–Jeans to Planck brightness temperature,[15] the seven seasonal *W*-band averages are shown in comparison to the Wright model predictions at 3.2 mm in Figure 3. This plot is similar to Figure 15 of Hill et al. (2009), whose preliminary analysis found that the Wright model was a good predictor of the mean temporal variation, but the model T_b seemed high by roughly 10%. Our results generally agree, but we find that multiplying the Wright model by a factor of 0.953 fits the seven-year data best. If one uses the Wright model tabulated at 350 μm, the plot looks nearly identical, but the scaling factor is 0.941, or about a 6% reduction. A previous comparison by Griffin et al. (1986) indicated that the 3 mm whole-disk observations of Ulich (1981) were within 7.5% of Wright model predictions at 350 μm. The first *WMAP* Mars observing season occurred during the time of the 2001 July–October massive global dust storm which elevated atmospheric temperatures in the mid-IR by nearly 40 K (Smith et al. 2002). The effect of dust storms on microwave data is expected to be less of a concern, but we did fit for the model scaling factor both with and without inclusion of the first observing season, with no significantly different results.

The uncertainties on the derived *WMAP* seasonal brightness temperatures increase with decreasing frequency, which follows as a result of decreasing signal-to-noise in the data. However, it is possible to extract a trend in temperature with frequency by finding within each season the ratio of the brightness temperature at each frequency to that at the W band, and then computing the mean over all seven observing seasons as a function of frequency. These means are plotted in Figure 4 in black. Errors are standard deviations of the mean. The weak frequency dependence can be characterized roughly as $\nu^{0.03}$, indicated by the blue line. The Wright model, processed in the same fashion, predicts almost no variation with frequency (red line). Such a frequency dependence could be attributed to an emissivity change of $\sim 5\% \pm 2\%$ over the wavelength interval. In a similar vein, a weak $5\% \pm 3\%$ decline in surface emissivity with increasing wavelength was noted by Burgdorf et al. (2000) in the 50 to 180 μm range, based on analysis of *Infrared Space Observatory* (*ISO*) observations of water vapor absorption lines.

Some consideration was given to placing the *WMAP* observations in a wider context, with the goal of gaining further insight into the model parameters. A search was made for a dataset that would provide absolutely calibrated, whole-disk observations of Mars which spanned both sides of the thermal energy distribution peak and were taken over a reasonably contiguous interval of time. Mars data taken by the *COBE*/DIRBE instrument (Boggess et al. 1992; Hauser et al. 1998) for a 146 day interval (1990 April 28–September 20) most closely matched these requirements, although no analysis of the publicly available[16] data appears to have been previously published. There are six DIRBE wavebands which sample the thermal emission portion of the Mars spectrum, with effective wavelengths of 12, 25, 60, 100, 140, and 240 μm. Of these, the

Table 6
Derived Mars Temperatures per Observing Season per Frequency

Season	RJD[a]	T_b(K)[b]				
		K	*Ka*	*Q*	*V*	*W*
1	2182.62	178 ± 4	182 ± 3	186 ± 4	191 ± 3	189 ± 2
2	2776.39	183 ± 4	187 ± 3	191 ± 4	197 ± 3	204 ± 2
3	2983.75	191 ± 4	195 ± 3	185 ± 4	193 ± 3	195 ± 2
4	3586.17	200 ± 3	199 ± 2	203 ± 3	209 ± 2	213 ± 1
5	3758.26	191 ± 5	184 ± 3	189 ± 4	186 ± 3	185 ± 2
6	4389.29	186 ± 4	187 ± 3	196 ± 4	197 ± 3	198 ± 2
7	4530.49	174 ± 6	177 ± 4	176 ± 5	181 ± 4	182 ± 2

Notes.
[a] Approximate mean time of observations in each season, Julian Day −2450000. Masking of data in proximity to Uranus and Neptune skews the mean data time of the second season toward the beginning of the observing season.
[b] Brightness temperature calculated for a solid angle $\Omega_{\mathrm{ref}} = 7.153 \times 10^{-10}$ sr at a fiducial distance of 1.5 AU. Temperature is with respect to blank sky: absolute brightness temperature is obtained by adding 2.2, 2.0, 1.9, 1.5, and 1.1 K in bands K, Ka, Q, V, and W, respectively (Page et al. 2003a)

[15] The Wright model predictions are tabulated as Planck brightness temperatures, which reconstruct the model flux assuming a blackbody with no limb darkening.

[16] http://lambda.gsfc.nasa.gov/

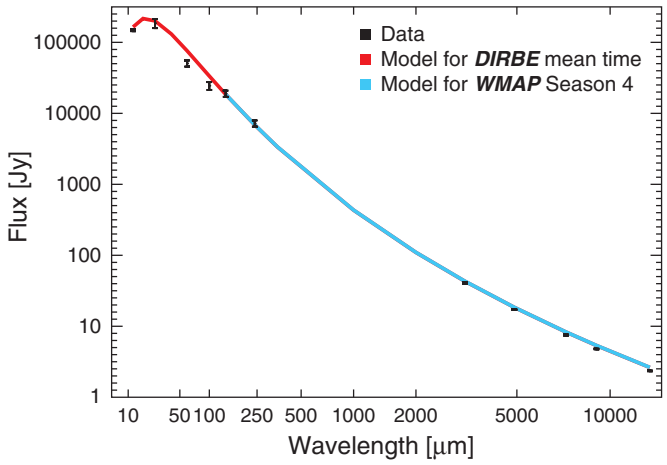

Figure 5. Mean Mars fluxes derived from DIRBE observations in 1990 and *WMAP* observing season 4 in 2005. Although separated by several years, the geometrical observing configuration is similar between the two dates, and the Wright model predictions (red and cyan lines) for the two time intervals for wavelengths between 140 μm and 1.3 cm overlay each other on this scale. DIRBE measurements for wavelengths $\leqslant$100 μm do not provide good constraints for testing model accuracy. The *WMAP* data lie a few percent below the model, which is significant given the error bars.

25 μm observations cannot be used as an independent check of the Wright model, since the model itself was the ultimate source of the DIRBE absolute calibration in this band (S. Moseley & W. Glaccum 2009, private communication; Hauser et al. 1998). In addition, while the 12, 25, 140, and 240 μm detectors are well-behaved linear devices, the 60 and 100 μm detectors are known to suffer nonlinear response, and Mars is on the bright end of that response. DIRBE is a broadband photometer, and reports monochromatic flux values at the effective wavelength of each band assuming a constant source spectrum in νI_ν across the band. One must apply a "color correction factor" to the reported fluxes if the source spectrum is different from that assumed. The DIRBE Explanatory Supplement provides such factors for gray-body and power-law spectra. However, in the case of Mars, some of the DIRBE bands intercept known atmospheric absorption lines. A significant CO absorption centered at 15 μm lies well within the 12 μm passband, and grazes the blue edge of the 25 μm band. Numerous minor water vapor absorptions are known to occur at wavelengths sampled by the 60 and 100 μm bands (Sidher et al. 2000). We have used spectral data available from the MGS thermal emission spectrograph (TES) public archives[17] and the *ISO* spectrum published by Sidher et al. (2000) to form approximate correction factors for the DIRBE data at these bands: only the 12 μm band required significant correction. For the 140 and 240 μm bands, color corrections were calculated using the spectrum predicted by the Wright model.

A mean flux at each DIRBE effective wavelength was evaluated over the 146 day interval, including application of color corrections and scaling to a fiducial solid angle at a distance of 1.5 AU (Table 7). Although the epochs of *WMAP* and DIRBE observations are separated by more than 10 years, the viewing geometry at the time of the DIRBE observations is most closely duplicated during *WMAP* observing season four. The *WMAP* mean brightness temperatures for this season were also converted to fluxes using the same fiducial solid angle, and both sets of data plotted as a spectrum in Figure 5. The spectra predicted by the Wright model for the mean time of the two epochs are also shown on the plot. For clarity, the quoted model errors of about $\pm$5% are not shown on the plot. On the logarithmic scale needed to show both sets of data together, the two model spectra overlay each other. Within the quoted data and model errors, the DIRBE measurements at 60 and 100 μm do not match well with the model. The DIRBE 12 μm data deviate by a little more than 1σ, accounting for both data errors and model accuracy. In the case of the 60 and 100 μm bands, we suspect a nonlinear response to a bright object is the root cause. The 12 μm band has a low absolute calibration error, but there is a significant and uncertain color correction due to the CO_2 atmospheric absorption. Ratios of the DIRBE fluxes to Wright model predictions are presented in Table 7; the major source of DIRBE error is that of the absolute calibration, which is also listed. DIRBE observations at 140 and 240 μm agree within the 10% calibration errors, but cannot be used to deduce any trend with frequency, such as seen by *WMAP*. We decided to forgo adjustments to the model at this point.

Table 7
COBE/DIRBE Mars fluxes[a]

λ (μm)	Flux (Jy)	Abscal Err[b] (%)	$F/F_{\rm model}$[c]
12	148594	3.1	0.89
25	186136	14.6	0.92
60	50606	10.0	0.66
100	24477	12.8	0.73
140	18991	10.1	1.02
240	7217	10.1	1.05

Notes.
[a] Fluxes have been averaged over the 146 day observing period, after correction to a fiducial distance of 1.5 AU and application of color corrections (see the text).
[b] Uncertainty in absolute calibration, as documented in the DIRBE Explanatory Supplement (Hauser et al. 1998).
[c] Ratio of observed DIRBE flux to Wright model prediction. The model is processed in the same manner as the data. Model uncertainty is quoted as roughly $\pm$5%.

As currently implemented, the Wright model may be used to predict microwave observations at *WMAP* frequencies by applying a "post-processing" multiplicative scaling factor to the published values: $T_{\rm new} = T_{\rm pub} \times f_{\rm scl}$. For both model and data evaluated at 3.2 mm, we have already noted a scaling factor of 0.953. We use the mean ratios of the remaining four frequencies to *W* band (Figure 4) as scaling factors for these frequencies, which are in Column 2 of Table 8. The W-band observations can be reproduced to $\sim$ 0.5%, with confidence decreasing with frequency to $\sim$ 2% at the K band. Since the 3.2 mm model values we have computed are not published, we also provide scaling factors to the 350 μm temperatures, which are derived from the the scaling factor of 0.941 noted earlier and multiplied through by the 3.2 mm scaling ratios.

Differences between measurements and the Wright model at *WMAP* wavelengths are not unexpected. The Wright model was designed to predict infrared emission arising from the top layer of the Martian surface, whereas the microwave signal originates from subsurface layers of order several centimeters deep (de Pater 1990; Orton & Burgdorf 2003), with potentially different composition and compaction. This was recognized by Griffin et al. (1986) and Griffin & Orton (1993), who recommended a logarithmic interpolation between the Wright 350 μm prediction and the 3.3 mm brightness temperature

[17] http://tes.asu.edu/

Table 8
Mars Model Scaling Factors for *WMAP* Frequencies

Freq.	f_{scl} (3.2 mm)[a]	f_{scl} (350μm)[b]	$\sigma_{f_{scl}}$(%)[c]
K	0.908	0.897	2
Ka	0.914	0.903	1
Q	0.923	0.912	1
V	0.943	0.932	0.7
W	0.953	0.941	0.5

Notes.
[a] Scaling factor applied to Wright model evaluated at 3.2 mm which will reproduce *WMAP* observational means at the specified frequencies.
[b] Scaling factor applied to Wright model evaluated at 350 μm which will reproduce *WMAP* observational means at the specified frequencies.
[c] Approximate 1σ error in both scaling factors.

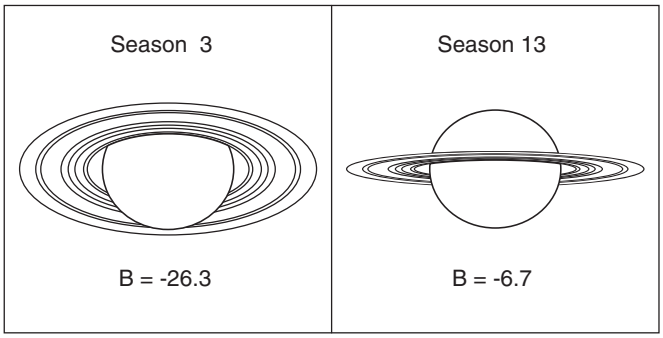

Figure 6. Extrema of Saturn viewing geometry sampled during the 14 observing seasons available in the seven-year *WMAP* data; *B* is the ring opening angle at mid-season. The contours illustrate the components used in an empirical model consisting of the planetary disk and seven ring regions, each of a different fixed normal optical depth. Only the A, B, C, and Cassini division rings are represented, and the radial divisions follow those used by Dunn et al. (2002).

versus Mars–Sun distance fit of Ulich (1981), citing agreement with the Rudy model within 1.2% for a dielectric constant revised upward from 2.25 to 2.8. On average, the Ulich (1981) fit predicts brightness temperatures roughly 5% higher than the *WMAP* mean seasonal values at 3.2 mm. This suggests that the lower value for the dielectric constant is preferable. We obtained disk-averaged Rudy model predictions at *WMAP* seasonal mean times of observation using a web-based, slightly revised version of the model maintained at NRAO.[18] In general, Rudy model predictions using the "standard dielectric constant" were slightly high compared to the *WMAP* observations, by $\sim$ 1% at 3.2 and 4.9 mm and roughly 3% at 7.3, 9.1, and 13.1 mm.

It should be noted that the *WMAP* observations provide model constraints only in the disk-averaged sense. The post-processing scaling of the Wright model suggested here simulates a frequency-dependent emissivity, which implies slow changes in mean subsurface properties with depth. In the Rudy model, which already incorporates subsurface sampling, use of model parameters derived from the radio data produces agreement with *WMAP* within a few percent. It is possible that this agreement could be improved either through the use of a revised dielectric function or updated thermal inertia and albedo maps. The thermophysical parameters used by the Rudy model are based on $\sim$20 year old maps of thermal inertia and albedo from the infrared thermal mapper (IRTM) on board *Viking* (Muhleman & Berge 1991). More recent MGS maps of these quantities obtained using the TES instrument are available with roughly 10 to 40 times better spatial resolution, full planet coverage and approximately twice the signal-to-noise (Christensen 1998; Christensen et al. 2001). The surface albedo has been observed to have some time dependence: a visual comparison between the *Viking* IRTM and TES albedo maps shows alterations in the spatial pattern have occurred since the *Viking* mapping (Christensen et al. 2001).

3.4. Saturn

As with Mars, Saturn's microwave brightness temperature varies considerably over time for near-Earth observers, primarily as a result of geometrical effects. Here the dominant factors are the observer's changing viewing angle of the rings and projected disk of the oblate planetary spheroid.

The ring system presents the main difficulty in Saturn's use as a calibrator in the microwave, although substantial progress has been made in understanding and modeling it. As evidenced by images from *Hubble Space Telescope* (*HST*) and data from orbiter and flyby missions such as *Cassini* and *Voyager*, Saturn's ring system is complex and rich in detail. The brightest rings (A, B, C) are composed of objects typically less than 5 m in size (Marouf et al. 1983) and are composed primarily of water ices mixed with a small amount of impurities (Poulet et al. 2003, and references therein). Those portions of the rings between the observer's line of sight and the planet serve to attenuate emission from Saturn's disk. The rings also contribute to the microwave signal via a mix of scattering and thermal re-emission of planetary radiation. The crossover point between the two emission mechanisms occurs near 1 cm (Dunn et al. 2002; Schloerb et al. 1980; Epstein et al. 1980), with thermal emission dominating shortwards and scattering longwards. Optical depths have been measured at a variety of wavelengths: Dowling et al. (1987) found that the optical depth of the combined ABC rings is roughly gray over a wide frequency range. *Voyager I* radio occultation observations (Tyler et al. 1983) at 3.6 and 13 cm produced radial profiles of optical depth for the A and C rings and Cassini division, but only approximate results for portions of the B ring with $\tau > 1$. The most complex and recent modeling of microwave data is that of Dunn et al. (2002, 2005, 2007) who use a Monte Carlo radiative transfer code to simulate the scattered and thermal emission of the rings based on VLA and other high-resolution observations.

WMAP does not spatially resolve the individual components of the Saturn system, nor is the spectral coverage sufficient to definitively isolate ring scattering and thermal spectral regimes. However, the changes in viewing geometry with orbital phase can be used to break degeneracy between ring and disk components, especially as the viewing aspect of the rings becomes more "edge-on". Over the currently available seven-year observing baseline, Saturn's rings are seen at inclinations between -28° and -6°: the sign convention indicates that the planet's south pole is tilting slowly away from the observer as the 0° edge-on equatorial configuration is approached. Figure 6 illustrates the two extrema and Table 9 list mean times and ring opening angles for each observing season.

Hill et al. (2009) briefly discussed *WMAP* five-year W-band observations of Saturn, which sampled ring opening angles $B \leqslant -17^\circ$. They found that the brightness temperature could be fit remarkably well with a simple $\sin B$ dependence. This convenient relationship does not effectively characterize the behavior at lower inclinations, however, and so a more complex

[18] Available at http://www.aoc.nrao.edu/~bbutler/work/mars/model/.

Table 9
Derived Saturn Temperatures per Observing Season per DA

Season[a]	RJD[b]	B[c]	T_b (K)[d]									
			K	Ka	Q1	Q2	V1	V2	W1	W2	W3	W4
1	2175.58	−26	133 ± 1	141 ± 1	146 ± 1	148 ± 1	157 ± 1	156 ± 1	164 ± 1	164 ± 1	166 ± 1	167 ± 1
2	2305.74	−25	133 ± 2	143 ± 1	146 ± 1	148 ± 1	155 ± 1	156 ± 1	161 ± 1	165 ± 1	164 ± 1	165 ± 1
3	2554.16	−26	131 ± 2	141 ± 1	149 ± 1	150 ± 1	158 ± 1	157 ± 1	166 ± 1	166 ± 1	164 ± 1	166 ± 1
5	2931.78	−24	131 ± 1	138 ± 1	144 ± 1	146 ± 1	153 ± 1	153 ± 1	161 ± 1	161 ± 1	160 ± 1	161 ± 1
7	3310.06	−21	126 ± 1	135 ± 1	140 ± 1	140 ± 1	147 ± 1	148 ± 1	154 ± 1	154 ± 1	154 ± 1	154 ± 1
8	3441.94	−23	130 ± 2	138 ± 1	142 ± 1	141 ± 1	149 ± 1	150 ± 1	155 ± 1	159 ± 1	159 ± 1	158 ± 1
9	3690.17	−17	122 ± 1	130 ± 1	135 ± 1	134 ± 1	141 ± 1	141 ± 1	146 ± 1	146 ± 1	147 ± 1	147 ± 1
10	3813.21	−20	125 ± 2	131 ± 1	132 ± 3	134 ± 3	143 ± 2	142 ± 1	150 ± 1	149 ± 2	148 ± 2	152 ± 2
11	4068.06	−12	123 ± 1	130 ± 1	132 ± 1	137 ± 1	139 ± 1	140 ± 1	142 ± 1	144 ± 1	143 ± 1	144 ± 1
12	4196.39	−15	121 ± 2	131 ± 2	132 ± 1	136 ± 1	139 ± 1	141 ± 1	143 ± 1	143 ± 1	143 ± 1	144 ± 2
13	4443.26	−6	128 ± 2	131 ± 1	135 ± 1	138 ± 1	140 ± 1	139 ± 1	143 ± 1	146 ± 1	142 ± 1	146 ± 1
14	4577.96	−9	123 ± 2	130 ± 1	132 ± 1	133 ± 1	140 ± 1	141 ± 1	140 ± 1	141 ± 1	141 ± 1	141 ± 1

Notes.
[a] Seasons 4 and 6 omitted from analysis because Saturn is aligned with the Galactic plane.
[b] Approximate mean time of observations in each season, Julian Day −2450000.
[c] Approximate mean ring opening angle for each season, degrees.
[d] Brightness temperature calculated for a solid angle $\Omega_{\rm ref} = 5.096 \times 10^{-9}$ sr at a fiducial distance of 9.5 AU. A correction for planetary disk oblateness has not been applied, as that is accounted for in modeling. Temperature is with respect to blank sky: absolute brightness temperature is obtained by adding 2.2, 2.0, 1.9, 1.5, and 1.1 K in bands K, Ka, Q, V, and W, respectively (Page et al. 2003a).

formulation is needed for the seven-year data. We adopt a simple empirical model of Saturn's microwave emission, variants of which have appeared in the literature for over 30 years (e.g., Klein et al. 1978; Epstein et al. 1980). The goal is to provide a predictive formula for the unresolved observed brightness of Saturn with as low an error as possible: however, given the *WMAP* data constraints, such a model will lack physical detail. At a given frequency ν, we assume a single temperature for the planetary disk, $T_{\rm disk}(\nu)$, and that all rings are characterized by the same temperature $T_{\rm ring}(\nu)$. The model variant we adopt allows for seven radially concentric ring divisions as defined by Dunn et al. (2002), which are based on optical depth variations observed by *Voyager* (Tyler et al. 1983). Each of the seven ring sectors has its own ring-normal optical depth $\tau_{0,i}$, with $1 \leqslant i \leqslant 7$, but each $\tau_{0,i}$ is assumed to be both constant within its ring and frequency independent.

Those portions of the planetary disk which are obscured by ring cusps will have their emission attenuated by a factor $e^{-\tau_{0,i}|\csc B|}$, where B is the ring opening angle seen by the observer. Thus at a given frequency and ring opening angle B:

$$T(\nu, B) = T_{\rm disk}(\nu)[A_{\rm ud} + \sum_{i=1}^{7} e^{-\tau_{0,i}|\csc B|} A_{{\rm od},i}] + T_{\rm ring}(\nu) \sum_{i=1}^{7} A_{r,i}, \quad (7)$$

where $A_{\rm ud}$, $A_{{\rm od},i}$ and $A_{r,i}$ are the projected areas of the unobscured disk, the portion of the disk obscured by ring i, and i^{th} ring, respectively. These areas are normalized to the total (obscured+unobscured) disk area. $T_{\rm ring}(\nu)$ is an observed brightness temperature and hides such physical details as ring emissivity and the apportionment of the scattering versus thermal emission. The assumption of a single mean ring temperature is a convenience rather than reality (Spilker et al. 2006; Grossman et al. 1989; Dunn et al. 2002). However, the apportionment between individual rings is not critical to the model fit, as it only depends on the summed total ring emission. Potential contributions to modeling error from nonuniform planetary disk emission are discussed later in this section.

Table 10
Saturn Model Fixed Parameters[a]

Ring Sector[b]	$R_{\rm inner}$ ($R^{\rm d}_{\rm Saturn}$)	$R_{\rm outer}$ ($R^{\rm d}_{\rm Saturn}$)	τ_0[c]
A	2.025	2.27	0.7
Cassini division	1.95	2.025	0.1
Outer B	1.64	1.95	2.0
Inner B	1.525	1.64	1.0
Outer C	1.43	1.525	0.1
Middle C	1.29	1.43	0.15
Inner C	1.24	1.29	0.08

Notes.
[a] Disk radii are specified in Table 2.
[b] Following Table IV of Dunn et al. (2002).
[c] Ring-normal optical depth.
[d] $R_{\rm Saturn}$ refers to the equatorial radius.

The *WMAP* brightness temperatures in Table 9 are sorted by frequency band and B and then a single simultaneous fit for the model parameters is made. Two separate fits were tried, differentiated from one another in the handling of the ring optical depth. In one fit, the $\tau_{0,i}$ were held fixed at the values chosen by Dunn et al. (2002; Table 10), and the ten disk and ring temperatures (for each of 10 DAs) were solved for. In an alternate fit, the relative ratios between the $\tau_{0,i}$ were fixed as per the table, but a single $\tau_{0,\rm max}$ was solved for in addition to the ten free temperatures. Both fits returned similar results, with reduced χ^2 of $\sim$ 1.2 for $\sim$ 100 degrees of freedom. We show only the results for the fixed-τ fit.

The disk and ring brightness temperatures derived from this model fit are presented in Table 11. Formal errors for the ring and disk temperatures at lower frequencies are higher because the ring contribution is smaller and there is a larger covariance between the two components. The model fit and residuals are shown in Figure 7. The model reproduces the observations to within $\sim$ 3%, but observations closer to $B = 0^\circ$ would better constrain the disk temperatures and so reduce the covariance between the disk and rings. The parameterization chosen for the

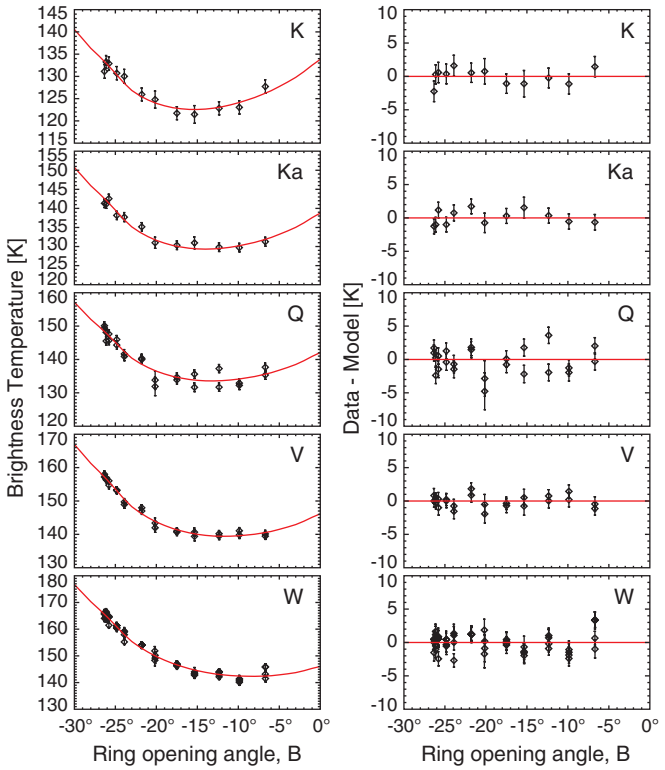

Figure 7. Modeling results for Saturn. Left: brightness temperatures based on unresolved Saturn observations as a function of ring inclination B are shown in black for each *WMAP* frequency band. Where there are multiple differencing assemblies per frequency, multiple points are plotted at each inclination. An empirical model including both ring and disk components (see the text) is overplotted in red. The temperature of the planetary disk predicted by the model occurs at $B = 0°$, when the rings are viewed edge-on. The model is symmetric about $B = 0°$. Right: residuals (data-model). The model predicts the observed brightness temperature within ≈3%.

Table 11
Saturn Model Fit Parameters

Freq.	Disk			Rings		
	T_{disk} (K)	σ_{fit} (K)	$\sigma_{adopted}$ (K)	T_{ring} (K)	σ_{fit} (K)	$\sigma_{adopted}$ (K)
K	133.8	1.5	4.0	6.7	1.1	2.1
Ka	138.8	1.2	3.7	9.6	0.8	1.8
Q	142.1	0.9	3.4	11.3	0.6	1.6
V	146.1	0.7	3.2	14.5	0.5	1.5
W	146.0	0.6	3.1	19.8	0.4	1.4

ring optical depths, together with the incomplete sampling of the ring system orientation, allows for alternate models which would fit the data equally well but return somewhat different mean disk and ring temperatures. This systematic is not reflected in the formal fitting errors in Table 11. In order to assess the magnitude of this error, we explored a small number of model variants. The model which fit the data equally well but returned temperatures with the largest differences compared to Table 11 consisted of a combined ABC ring represented by a single τ_0, which was a free parameter in the fit. Disk temperatures derived for this model were ∼ 2.5 K higher, and ring temperatures ∼1 K lower. As a conservative approach, we additively combine this estimated systematic error with the formal fitting errors to produce the "adopted error" columns in Table 11. The derived disk and ring temperatures match well with those already in the literature. Figure 8 shows the *WMAP* derived disk temperatures

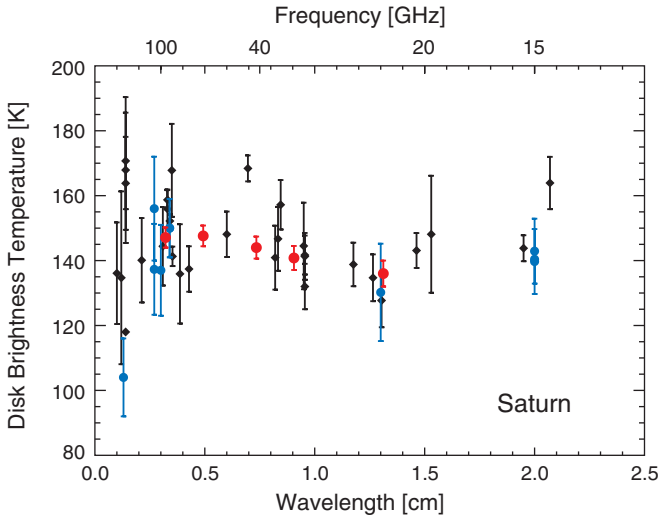

Figure 8. Spectrum of Saturn's disk. Black diamonds are from Klein & Gulkis (1978), consisting of a compendium of unresolved observations which were corrected for a ring contribution. Filled blue circles are interferometric observations from Grossman et al. (1989), de Pater & Dickel (1991), and Dunn et al. (2005). Red circles are disk temperatures derived from *WMAP* data using an empirical model to separate disk and ring contributions. *WMAP* disk temperatures are corrected to absolute brightness. The *WMAP* values agree with the interferometric observations within the uncertainties, while providing tighter constraints at multiple frequencies. Uncertainties in the *WMAP*-derived disk temperatures are expected to decrease when observations at ring inclinations near 0° become available. Ammonia absorption near 24 GHz is less pronounced for Saturn than for Jupiter, making tighter constraints useful.

in context with the compendium of Klein et al. (1978) plus more recent interferometric observations. The ring temperatures also compare well with those measured directly from high-resolution images of the ring ansae (Dunn et al. 2005; Schloerb et al. 1980; Janssen & Olsen 1978): see Figure 9. Figure 10 illustrates the percentage contribution of the ring to our total model, which sums the ring emission and attenuation of disk radiation, as a function of frequency and ring inclination B.

The empirical model described here assumes Saturn's mean whole-disk temperature is time invariant at each frequency. The presence of band-like structures (which can persist for years) and latitudinal brightness gradients at the ∼5% level have been noted by several observers at wavelengths of 2 cm and longward (Grossman et al. 1989; de Pater & Dickel 1991; van der Tak et al. 1999). There is less discussion in the literature of disk temperature structure and/or variability at the frequencies observed by *WMAP*: there have been no reports of bands or localized structures, but some indication of north/south latitudinal brightness differences. Within the seven-year epoch under consideration, Dunn et al. (2005) observed a latitudinal disk brightness gradient at 3 mm, such that the north pole was brighter than the south by ∼5%. They interpreted differences between their 1.3 mm and 3 mm data, taken roughly 4 months apart, as possible evidence for atmospheric changes on week to month timescales. In order to estimate potential model bias caused by the assumption of a uniform disk temperature, Saturn seasonal brightness temperatures were simulated using geometrical models similar to those described in this section, with the addition of a disk latitudinal gradient as described by Dunn et al. (2005). If one makes the assumption that such a temperature gradient is persistent over seven years and exists at all *WMAP* frequencies, then such structure would produce a temperature behavior with inclination which is asymmetric

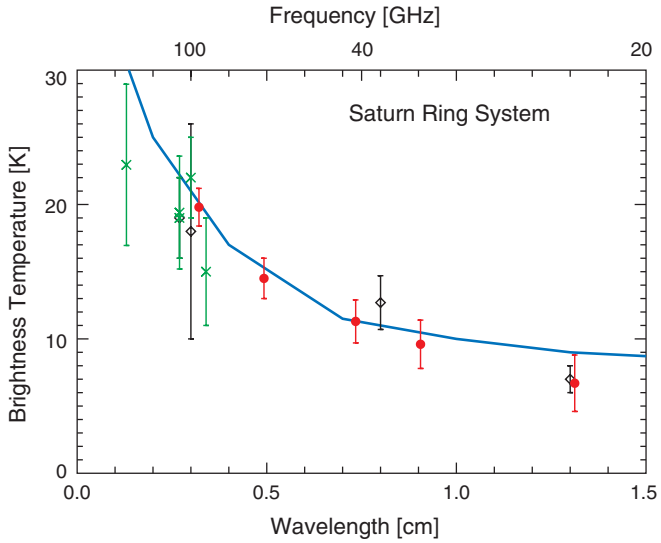

Figure 9. Brightness temperature of Saturn's combined rings. Interferometric measurements taken from Table 4 of Dunn et al. (2005) are shown in green. Black points are older observations from Janssen & Olsen (1978) and Schloerb et al. (1980). Model predictions from Figure 7 of Dunn et al. (2005) are plotted as the blue line. The derived *WMAP* ring temperatures, shown in red, compare well with the observations of others and the Dunn et al. model. Results from Dunn et al. (2002) indicate that the rings primarily scatter rather than absorb CMB radiation; thus ring temperatures have not been corrected to absolute brightness as is necessary for the disk temperatures.

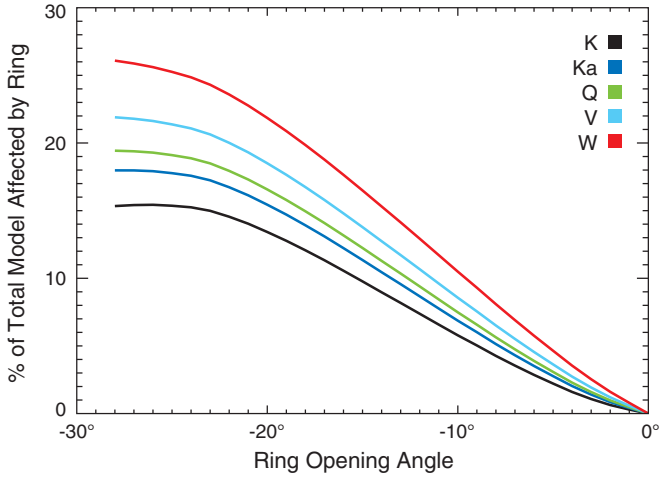

Figure 10. Contribution of ring emission plus ring-attenuated disk emission to the total computed brightness temperature of Saturn, expressed as a percentage. Exact values are model dependent; this set is for the empirical model discussed in the text, and whose parameters are given in Tables 10 and 11. The ring system contribution is lowest in the K band, where thermal emission is dropping and scattering is more dominant.

about $B = 0°$. This is because the rings would obscure hotter regions in the northern portion of the disk but colder regions in the south, producing a maximum deviation from symmetry of ∼1% at the largest ring opening angles. Since the *WMAP* seven-year observations sample slightly less than half of the full B range, this asymmetry would not be evident, and a model fit which assumes a constant disk temperature would use the ring model component to compensate for the disk temperature gradient. For a simulated dataset matching the *WMAP* seven-year observing seasons, the model fit returns a mean ring temperature biased by less than 1 K, with an unbiased recovery of the mean whole-disk temperature. This estimate is of uncertain quality, however, because it is based on a snapshot of Saturn at one wavelength and a narrow time window. For this reason, the adopted errors in Table 11 have not been adjusted to reflect this potential effect.

An extended, low optical depth dust ring associated with Saturn's moon Phoebe was recently discovered using *Spitzer* imaging at 24 and 70 μm (Verbiscer et al. 2009). With a quoted radial extent between at least 128 and 207 Saturn radii, or roughly 1° in apparent diameter, it would be possible for *WMAP* to resolve the Phoebe ring, with *W* band as the best chance for doing so. However, no signal from the ring was detected by *WMAP*. Properties of the grains are not well specified, but naive estimates assuming typical dust emission and optical depth frequency dependencies would predict temperatures at 94 GHz of less than 1 μK, well below achievable noise levels of about 300 μK (1σ).

3.5. Uranus and Neptune

With their lower brightness, lack of a dominant ring system, and small solid angle, Uranus and Neptune are used as primary calibrators in infrared through radio wavebands for both ground- and space-based instruments. Spectral coverage in the microwave is somewhat undersampled, however, leaving room for interpretation in atmospheric modeling efforts. The microwave spectra of Uranus and Neptune lack the broad NH_3 absorption centered near 24 GHz which is characteristic of Jupiter and Saturn. At millimeter wavelengths, collision-induced absorption by H_2 is considered the dominant continuum opacity source. CO rotational absorptions have been observed for Neptune in the sub-millimeter (Marten et al. 2005). At centimeter wavelengths, ammonia (which is depleted relative to solar nitrogen levels) and hydrogen sulfide are the main opacity contributors (Deboer & Steffes 1996; Spilker 1995; de Pater et al. 1991). Of special note is Uranus' unique 98° obliquity, which allows for a slowly changing pole-to-pole panorama of the planet as it moves in its 84 year orbit, and may also play a role in determining atmospheric conditions.

For selected frequencies, observational databases spanning decades have permitted characterization of the variability of these two planets. Uranus in particular has exhibited long-term whole-disk temperature changes since 1966 which correlate with the viewing aspect of the south pole. After accounting for geometrical solid angle changes, Kramer et al. (2008) reported a gradual temperature drop of order 10% over 20 years (1985–2005) at 90 GHz. This is interpreted as a true integrated-disk temperature change, as the 1985 face-on contribution from the bright south pole progressively morphs into a 2007 view dominated by colder equatorial regions. Similar findings, with similar phasing albeit different amplitudes, have been reported in the radio (Klein & Hofstadter 2006) and visible (Hammel & Lockwood 2007). There is weaker evidence that some portion of variability in the light curves is attributable to changes deep in the atmosphere (Klein & Hofstadter 2006); Hofstadter & Butler (2003) used VLA 2 and 6 cm "snapshots" of the disk over several years to argue for opacity changes in zonal bands. Neptune's microwave variability is less well documented, although there is ample evidence for variability in the visible and near-IR, as summarized by Hammel & Lockwood (2007). Kramer et al. (2008) find the 90 GHz integrated disk temperature to be constant to within ∼8% over 20 years.

Peak *WMAP* antenna temperatures for these distant "ice giants" range from roughly 1 mK at the W band to ∼0.2 mK

Table 12
Derived Uranus Temperatures per Observing Season per Frequency

Season	RJD[a]	D_W[b]	T_b(K)[c]				
			K	*Ka*	*Q*	*V*	*W*
1	2204	−26.4	163 ± 45	89 ± 34	133 ± 25	107 ± 18	144 ± 15
2	2437	−19.0	192 ± 37	139 ± 28	135 ± 24	162 ± 17	130 ± 15
3	2573	−22.4	172 ± 41	150 ± 31	193 ± 22	117 ± 18	110 ± 15
4	2807	−15.2	148 ± 57	68 ± 44	193 ± 34	132 ± 31	66 ± 25
5	2942	−18.5	189 ± 58	94 ± 43	147 ± 31	143 ± 25	106 ± 21
6	3176	−11.2	192 ± 37	97 ± 28	144 ± 22	177 ± 19	141 ± 16
7	3312	−14.5	146 ± 38	148 ± 29	122 ± 23	160 ± 18	117 ± 15
8	3546	−7.3	121 ± 37	116 ± 28	167 ± 23	109 ± 18	108 ± 14
9	3681	−10.7	175 ± 38	117 ± 29	127 ± 22	134 ± 18	112 ± 15
10	3915	−3.4	167 ± 37	87 ± 28	117 ± 22	157 ± 18	137 ± 15
11	4050	−6.7	139 ± 38	116 ± 29	148 ± 23	124 ± 18	138 ± 15
12	4284	0.5	148 ± 37	152 ± 28	161 ± 21	143 ± 18	114 ± 15
13	4419	−2.8	246 ± 40	167 ± 30	203 ± 23	138 ± 19	120 ± 16
14	4654	4.4	135 ± 37	173 ± 29	167 ± 22	129 ± 18	97 ± 15
MEAN	...	...	166 ± 11	126 ± 9	153 ± 6	138 ± 5	120 ± 4

Notes.
[a] Approximate mean time of observations in each season, Julian Day −2450000
[b] Sub-*WMAP* latitude, degrees.
[c] Brightness temperature calculated for a solid angle $\Omega_{ref} = 2.482 \times 10^{-10}$ sr at a fiducial distance of 19.0 AU. Temperature is with respect to blank sky: absolute brightness temperature is obtained by adding 2.2, 2.0, 1.9, 1.5, and 1.1 K in bands K, Ka, Q, V, and W, respectively (Page et al. 2003a).

Table 13
Derived Neptune Temperatures per Observing Season per Frequency

Season	RJD[a]	D_W[b]	T_b(K)[c]				
			K	*Ka*	*Q*	*V*	*W*
1	2185	−27.4	279 ± 106	126 ± 81	13 ± 65	78 ± 49	199 ± 42
2	2420	−27.9	303 ± 91	43 ± 70	191 ± 54	134 ± 41	197 ± 36
3	2555	−27.6	205 ± 106	27 ± 82	75 ± 60	72 ± 45	132 ± 38
4	2799	−27.9	137 ± 119	108 ± 90	120 ± 68	164 ± 54	152 ± 46
5	2923	−27.6	167 ± 102	146 ± 77	76 ± 66	178 ± 48	133 ± 39
6	3155	−28.0	24 ± 90	21 ± 70	188 ± 52	310 ± 43	151 ± 37
7	3290	−27.7	216 ± 91	121 ± 69	−14 ± 59	194 ± 51	196 ± 41
8	3522	−28.0	246 ± 93	180 ± 73	137 ± 52	53 ± 43	128 ± 36
9	3657	−27.9	184 ± 96	263 ± 74	140 ± 55	18 ± 51	154 ± 41
10	3890	−27.9	177 ± 96	150 ± 74	235 ± 55	131 ± 40	76 ± 36
11	4025	−27.9	89 ± 107	195 ± 83	151 ± 54	181 ± 48	162 ± 42
12	4257	−27.7	104 ± 93	232 ± 72	52 ± 54	161 ± 42	82 ± 38
13	4391	−27.6	−86 ± 116	193 ± 88	125 ± 57	161 ± 49	132 ± 42
14	4625	−27.6	142 ± 90	242 ± 68	180 ± 53	82 ± 46	116 ± 40
MEAN	...	...	161 ± 27	147 ± 21	126 ± 15	138 ± 12	142 ± 11

Notes.
[a] Approximate mean time of observations in each season, Julian Day −2450000
[b] Sub-*WMAP* latitude, degrees.
[c] Brightness temperature calculated for a solid angle $\Omega_{ref} = 1.006 \times 10^{-10}$ sr at a fiducial distance of 29.0 AU. Temperature is with respect to blank sky: absolute brightness temperature is obtained by adding 2.2, 2.0, 1.9, 1.5, and 1.1 K in bands K, Ka, Q, V, and W, respectively (Page et al. 2003a).

at the K band. The signal-to-noise for individual observations of these objects is low (∼0.3 at the W band, ∼0.14 at the K band), resulting in large statistical errors in single-season disk temperature determinations. Tables 12 and 13 present the single-season brightness temperatures computed for Uranus and Neptune. Brightness temperatures are listed per frequency rather than per DA as a means of boosting signal-to-noise for those frequencies with multiple DAs. Temperatures for Uranus observing seasons four and five exhibit somewhat larger error bars than other seasons. For these two seasons, there was a reduction in the number of observations available for analysis because data quality checks excluded observations in close proximity to Mars sky coordinates.

Sub-*WMAP* latitudes for Uranus range between −30° and 4° over our seven-year baseline. Linear correlations of T_b against both sub-*WMAP* latitude and time produced no statistically significant trend other than a flat line. This is not surprising given that the tightest seasonal temperature errors are of order 10%, which encompasses the entire twenty-year range of variation seen in the 90 GHz light curves of Kramer et al. (2008). We performed similar correlations for Neptune, with again the same null variability result. Note, however, that the sub-*WMAP* latitude for this planet is relatively unchanged over the epochs of observation. With no discernable variability over the observing baseline, we computed seven-year means of the disk brightness for each planet; these are listed as the last line in Tables 12 and 13. These seven-year means in turn may be compared to observations in the literature and placed in context with the microwave spectra in general.

Figure 11 overplots the seven-year mean *WMAP* Uranus temperatures at K, Ka, Q, V, and W center frequencies on a composite spectrum derived from several sources in the literature. Points are color-coded to reflect the decade in which observations were taken. Data have been culled from Griffin & Orton (1993), Muhleman & Berge (1991), Greve et al. (1994), Cunningham et al. (1981), and Gulkis et al. (1978). Also included is the mean 3.5 cm value from the 1966–2002 compilation of Klein & Hofstadter (2006), with a single large error bar indicating the ∼30 K peak-to-peak variation in the light curve. Within the quoted errors, there is general agreement between the *WMAP* observations and those taken at previous epochs. The *WMAP* observations show a "dip" in Ka-band temperature compared to neighboring frequencies. Although not of high statistical significance, a feature of this nature is clearly of interest. A literature search for corroborating observations near 30 GHz only returned those few acquired in the late 1960s, listed in Table 1 of Gulkis et al. (1978). For a variety of reasons, more recent observations would be preferable, but the older epoch does have the advantage of sharing a similar viewing geometry to that of the *WMAP* data. These older observations are plotted in gray in the Figure, and agree well with the *WMAP* measurements, but also do not define a "dip" at high statistical significance. Although suggestive of an interesting atmospheric opacity constraint for future study, the possibility of such a feature has gone unremarked in the literature.

A composite microwave spectrum for Neptune is shown in Figure 12. The color coding again indicates observational epoch, with ground-based data taken from de Pater & Richmond (1989), de Pater et al. (1991), Muhleman & Berge (1991), Griffin & Orton (1993), Hofstadter (1993), and Greve et al. (1994). Deboer & Steffes (1996) provide a summary of observations in the 1990s. Observations with error bars larger than about 30 K are not included in the plot. *WMAP*-derived temperatures for the Q band agree well with those of Greve et al. (1994), while the 94 GHz observations lie on the upper envelope of data taken in the 1970s and 1980s. *WMAP* observations occur when Neptune's south pole is most fully viewable. The observational error on the seven-year W-band mean is ∼8%, which is equivalent to the level to which Klein & Hofstadter (2006) claimed 20 year stability.

Reasonable temperature error bars for the *WMAP* Uranus and Neptune observations are only achieved through averaging the seven-year data. Observers wishing to use these data for

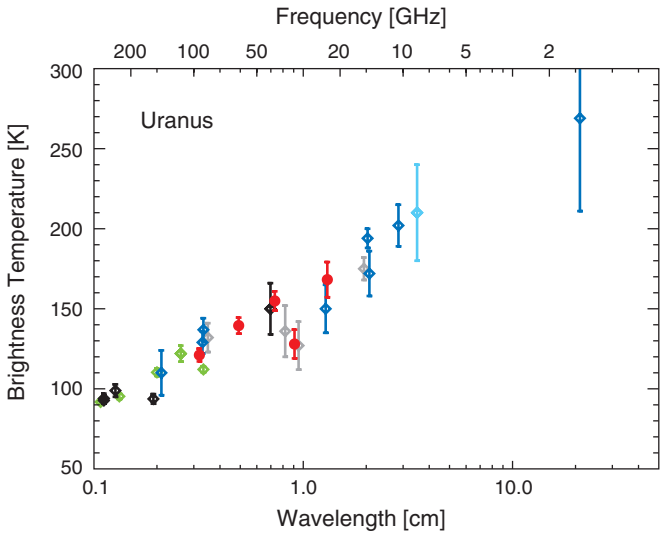

Figure 11. Microwave spectrum of Uranus, compiled from selected observations in the literature. Points have been color-coded into wide bins of observational epoch: gray for 1966–1969, blue for 1970–1979, green for 1980–1989, black for 1990–1999, red for *WMAP* points (2001–2008) and cyan for the 1966–2002 mean and peak-to-peak variability observed at 3.5 cm by Klein & Hofstadter (2006). See the text for detailed data references. *WMAP* data have been corrected to absolute brightness. Of potential atmospheric modeling interest is the "dip" near 30 GHz.

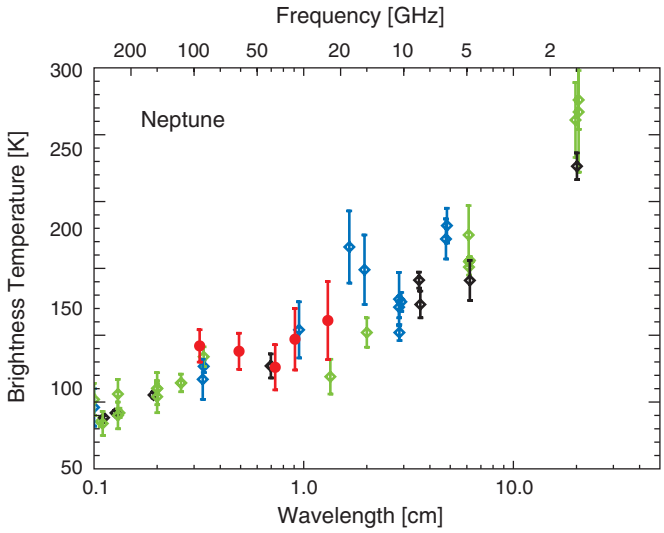

Figure 12. Microwave spectrum of Neptune, compiled from selected observations in the literature (see the text). Points have been color-coded into wide bins of observational epoch: blue for 1969–1979, green for 1980–1989, black for 1990–1999, and red for *WMAP* points (2001–2008). *WMAP* data have been corrected to absolute brightness, and in general agree well with previously published values.

calibration of observations taken outside of the 2001–2008 epoch should keep in mind the variability and related geometric issues described above.

4. CELESTIAL SOURCES

Non-variable, spatially isolated fixed celestial calibrators for millimeter wavelengths are not common. At high Galactic latitude, bright sources are predominantly identified as some form of AGN/QSO, which are prone to outbursts and variability on a wide range of timescales and frequencies. Brighter sources in the Galactic plane tend to be H II regions (which may not be "point-like") or supernova remnants (SNRs) with potential variability. At moderate spatial resolution, confusion with neighboring diffuse and compact sources in the Galactic plane can be an issue for background subtraction.

Five sources were chosen for study out of an original list which included some of the brightest sources from Baars et al. (1977) and Ott et al. (1994), in addition to the brightest, least variable objects from the seven-year *WMAP* source catalog (Gold et al. 2011). The five selected sources are listed in Table 14. Some of the sources which were initially considered but ultimately rejected, primarily because of low background contrast, included 3C286, NGC 7027, 3C84, 3C218, 3C123, and 3C147. There are unfortunately few suitable calibration sources in the Southern hemisphere with a long-term history of observation.

4.1. Data Processing and Analysis Methods

Flux densities of the selected sources are measured from the seven-year sky maps at HEALPix[19] resolution 9 (Nside = 512). For each frequency band, the azimuthally symmetrized beam profile (see Section 3.1) is convolved with a sky map pixel to produce a map-based beam template. The sum of the pixel-convolved beam template plus a sloping planar base level is fit to the Stokes *I*, *Q*, and *U* sky map data at each source position, using pixels within 3.5 times the beam width σ (1.5 times the FWHM) in each band. The peak source temperature from each fit is converted from thermodynamic temperature to Rayleigh–Jeans brightness temperature and then translated to a source flux density using a conversion factor Γ that is a weak function of the source spectral index (Jarosik et al. 2011). For point sources, this method of flux measurement is more accurate than the aperture photometry method as used for example by Page et al. (2003b) for Tau A. The *WMAP* beam profiles have extended wings (Hill et al. 2009), so an aperture radius $\gtrsim$3 times the beam FWHM should be used and the results are more susceptible to error due to background confusion.

The uncertainty in flux density is calculated as the quadrature sum of (1) map measurement uncertainty, (2) the uncertainty in Γ (0.5% to 0.7% depending on the band), and (3) the 0.2% absolute calibration uncertainty. For Stokes *I*, map measurement uncertainty is estimated from the rms fit residual in the fit region. The Stokes *I* residuals generally appear to be dominated by beam asymmetry effects, but also include background confusion and noise. (The source profiles in the maps are asymmetric due to asymmetry in the instantaneous beam profiles and the nonuniform distribution of scan angles over a year for sources away from the ecliptic poles.) For Stokes *Q* and *U*, map measurement uncertainty is calculated either from the 1σ source peak uncertainty and base level uncertainty from the beam fitting or as the *Q* or *U* flux times the fractional map measurement uncertainty for *I*, whichever is largest. The latter method is the estimated uncertainty in *Q* or *U* due to beam asymmetry effects, assuming the fractional uncertainty is the same in *Q* or *U* as it is in *I*. The flux determination was tested on simulated sky maps containing a population of point sources with no other signals and no noise, generated using *WMAP* beam window functions as described in Wright et al. (2009). Recovered flux densities were accurate to about 0.1% or better, except in W band where

[19] *WMAP* sky map products are in HEALPix format; see http://healpix.jpl.nasa.gov/. HEALPix divides the sky into pixels of equal area. The number and spacing between pixel centers depends on the chosen resolution. Nside = 512 corresponds to a pixel area of $\sim 3.995 \times 10^{-6}$ sr, with a mean spacing of 6.87 arcmin between pixel centers.

Table 14
Selected Celestial Calibration Sources

Source Name	R.A.$_{J2000}$ [a] (hms)	Decl.$_{J2000}$ (dms)	l (deg)	b (deg)	Type	Angular Extent (arcmin)	Reference
Cas A	23 23 24	+58 48 54	111.74	−2.13	Shell-type SNR	5	Green (2009)
Cyg A	19 59 28	+40 44 02	76.19	5.76	Radio galaxy	2.8 × 0.8	Ott et al. (1994)
Tau A (Crab)	05 34 32	+22 00 52	184.56	−5.78	Filled-center SNR	7 × 5	Green (2009)
3C58	02 05 38	+64 49 42	130.72	3.08	Filled-center SNR	9 × 5	Green (2009)
3C274 (M87, Vir A)	12 30 49	+12 23 28	283.78	74.49	Radio galaxy	2.5	Ott et al. (1994)

Notes. [a] Positions for the galaxies are from NED (http://nedwww.ipac.caltech.edu/) and positions for the SNRs are from SIMBAD (http://simbad.u-strasbg.fr/simbad/).

the recovered fluxes tended to be larger than the input fluxes by up to 1%. This is allowed for by including an additional 1% uncertainty term in the quadrature sum for W band.

Fractional year-to-year variability for the selected sources has been obtained using sky maps for individual years 1–7. To remove confusion noise from the CMB and Galactic foregrounds, we subtract the seven-year average map from each individual year map for each band. A pixel-convolved beam plus flat base level is fit to each difference map at each source position, giving a flux difference ΔF_i for the ith year for each source in each band. Uncertainty in ΔF_i is calculated from the quadrature sum of the source peak uncertainty and the base level uncertainty. The flux difference is divided by the mean flux from the seven-year map to get the fractional flux variation $\Delta F_i/\langle F\rangle$. For K, Ka, and Q bands, there is a small ($\lesssim$0.2%) but significant year-to-year variation in the *WMAP* calibration, which we have measured by correlating each yearly map against the seven-year map (see Figure 1 of Jarosik et al. 2011). The measured fractional flux variations in *K*–*Q* bands are corrected for these calibration variations c_i using $(\Delta F_i/\langle F\rangle)_{\rm corrected} = (\Delta F_i/\langle F\rangle)_{\rm measured} + (1 - c_i)$.

4.2. Results

Source flux densities from the seven-year maps are presented in Table 15. Fractional uncertainties for the Stokes *I* fluxes are typically 1 to 3%. For some of the sources, the maximum source extent given in Table 14 is not entirely negligible relative to the *WMAP* beam width in the V or W band (FWHM 19.′6 in V, FWHM 12.′2 in W, Hinshaw et al. 2009). We have estimated the possible error due to source extent for Tau A. The 1.4 GHz map of the Tau A region from the NVSS survey (beam size 45″ FWHM, Condon et al. 1998) was smoothed with the symmetrized *WMAP* V- or W-band beam and converted to a resolution 9 (Nside = 512) HEALPix map. The flux determined by our method was found to underestimate the true flux by 1.5% in *V* band and 3.7% in the W band. Spatial variations of the spectral index over Tau A are very small (Morsi & Reich 1987; Bietenholz et al. 1997; Green et al. 2004) so the source extent at *W* band is probably similar to that at 1.4 GHz. Our V- and W-band fluxes for Cas A and 3C58 may also be underestimated by similar amounts. To allow for this, the uncertainty values listed for these three sources in Table 15 include additional contributions of 1.5% in V and 3.7% in W, added in quadrature to the uncertainties calculated as described in Section 4.1.

Fractional year-to-year variability results are presented in Figure 13 and Table 16. Significant secular decrease is seen for Cas A and Tau A. The results are consistent with a frequency independent decrease of about 0.53% per year for Cas A and 0.22% per year for Tau A. Our results for Cas A fall between the ∼ 0.6% per year decrease found by O'Sullivan & Green (1999) near 15 GHz from 1965 to 1995 and the 0.394% ± 0.019% decrease found by Hafez et al. (2008) at 33 GHz from 2001 to 2004. Dependence of the Cas A decrease on frequency and epoch has recently been discussed by Reichart & Stephens (2000) and Hafez et al. (2008). For Tau A, we find a somewhat higher rate of decrease than that of 0.18% ± 0.01% per year found by Vinyaikin & Razin (1979a, 1979b) at 927 MHz from 1962 to 1977 and 0.167% ± 0.015% per year found by Aller & Reynolds (1985) at 8 GHz from 1968 to 1984. Hafez et al. (2008) found a decrease of 0.22% ± 0.07% per year at 30 GHz from 2002 January to 2004 September.

No significant secular trends are seen for the other sources, with 3σ upper limits in the K band of 0.12% per year for Cyg A, 0.21% per year for 3C58, and 0.54% per year for 3C274. The limit for Cyg A is consistent with the limit of 0.10% per year found by Hafez et al. (2008) at 33 GHz for the period 2001 March to 2004 May. For 3C58, Green (1987) reported an increase of 0.32% ± 0.13% per year at 408 MHz from 1967 to 1986.

Significant yearly flux variation is not seen for Cyg A and 3C58; the rms year-to-year variation is consistent with the uncertainties in each band. The lowest rms variation is in the K band, and is 0.27% for Cyg A and 0.33% for 3C58. Carilli & Barthel (1996) give an upper limit of 10% on Cyg A core variability from observations at 5, 15, and 90 GHz over timescales from 10 months to 15 years. The core contributes ⩽10% of the total flux at *WMAP* frequencies (e.g., Robson et al. 1998). For 3C274 there is evidence for year-to-year variability of about 2% in the K, Ka, and Q bands. The rms variation is 1.8 to 2.6 times the mean uncertainty in these bands, and the variations are correlated from band to band. Previous observations of 3C274 have shown greater variability. At 90 GHz, Steppe et al. (1988) reported a decrease of 1.4 Jy for the core between 1985 June and 1986 August, which corresponds to ∼17% of the total source flux. At 43 GHz, VLBA monitoring showed an increase of 0.57 Jy for the core region between 2008 January and April (Wagner et al. 2009), which corresponds to 4% of the total flux. Smaller core flux variations, less than 1% of the total flux, have been observed at lower frequencies (Morabito et al. 1988; Junor & Biretta 1995; Harris et al. 2009).

Spectra of the seven-year *WMAP* fluxes together with previous measurements from the literature are shown in Figures 14–18. For Cas A, we have scaled the *WMAP* fluxes, the Archeops fluxes of Desert et al. (2008), the SCUBA fluxes of Dunne et al. (2003), and the BLAST fluxes of Sibthorpe et al. (2010) to epoch 2000 using a secular variation of −0.53% per year. These are plotted with previous measurements that were scaled to epoch 2000 by Hafez et al. (2008) using frequency-dependent scaling. For Tau A, we have scaled previous measurements from Macias-Perez et al. (2010) to the epoch of the *WMAP* data using a secular variation of −0.167% per year at

Table 15
Flux Densities of Celestial Calibration Sources

Source	$\nu_{\rm eff}$[a] (GHz)	Γ[a] (mK Jy^{-1})	I Flux (Jy)	Q Flux (Jy)	U Flux (Jy)	P Flux[b] (Jy)	P/I[b] (%)	Pol Angle[c] (deg)
Cas A	22.68	0.2497	232.1 ± 2.9	−0.92 ± 0.09	−0.15 ± 0.09	0.93 ± 0.09	0.41 ± 0.04	85.5 ± 2.7 (66.0)
Cas A	32.94	0.2041	179.8 ± 1.5	−0.56 ± 0.08	−0.19 ± 0.09	0.59 ± 0.08	0.33 ± 0.05	80.6 ± 4.2 (61.1)
Cas A	40.62	0.2162	153.7 ± 1.5	−0.50 ± 0.09	−0.17 ± 0.10	0.53 ± 0.09	0.35 ± 0.06	80.6 ± 5.3 (61.1)
Cas A	60.48	0.2084	116.3 ± 2.0[d]	−0.25 ± 0.16[d]	0.12 ± 0.16[d]	0.28 ± 0.16	0.24 ± 0.14	−77.6 ± 16.8 (82.9)
Cas A	92.90	0.1800	84.0 ± 3.4[e]	−0.05 ± 0.28[e]	0.12 ± 0.28[e]	0.13 ± 0.28	0.16 ± 0.34	−56.1 ± 59.9 (104.4)
Cyg A	22.65	0.2493	57.7 ± 1.3	0.02 ± 0.05	−0.48 ± 0.06	0.48 ± 0.06	0.84 ± 0.11	43.6 ± 2.9 (164.8)
Cyg A	32.91	0.2039	38.2 ± 0.6	0.40 ± 0.08	0.20 ± 0.10	0.45 ± 0.08	1.18 ± 0.22	−13.5 ± 6.0 (107.7)
Cyg A	40.58	0.2159	29.8 ± 0.4	0.58 ± 0.08	0.18 ± 0.10	0.61 ± 0.09	2.04 ± 0.29	−8.4 ± 4.8 (112.8)
Cyg A	60.42	0.2083	18.6 ± 0.2	0.38 ± 0.15	0.26 ± 0.20	0.46 ± 0.17	2.48 ± 0.89	−16.9 ± 11.4 (104.3)
Cyg A	92.83	0.1802	11.1 ± 0.3	0.26 ± 0.26	0.11 ± 0.34	0.28 ± 0.27	2.55 ± 2.45	−11.5 ± 33.2 (109.7)
Tau A	22.70	0.2501	383.8 ± 9.6	−27.13 ± 0.68	1.40 ± 0.08	27.17 ± 0.68	7.08 ± 0.25	−88.5 ± 0.1 (149.1)
Tau A	32.96	0.2043	342.8 ± 6.4	−23.72 ± 0.45	1.88 ± 0.12	23.80 ± 0.44	6.94 ± 0.18	−87.7 ± 0.1 (149.9)
Tau A	40.64	0.2163	317.7 ± 8.6	−22.03 ± 0.60	2.06 ± 0.14	22.12 ± 0.60	6.97 ± 0.27	−87.3 ± 0.2 (150.3)
Tau A	60.53	0.2085	276.0 ± 5.2[d]	−19.25 ± 0.36[d]	1.52 ± 0.24[d]	19.31 ± 0.36	7.00 ± 0.19	−87.7 ± 0.4 (149.9)
Tau A	92.95	0.1798	232.8 ± 9.7[e]	−16.58 ± 0.73[e]	0.75 ± 0.42[e]	16.60 ± 0.73	7.13 ± 0.43	−88.7 ± 0.7 (148.9)
3C58	22.70	0.2500	20.8 ± 0.4	1.11 ± 0.04	0.45 ± 0.06	1.20 ± 0.05	5.77 ± 0.25	−11.0 ± 1.4 (5.4)
3C58	32.96	0.2043	19.0 ± 0.3	1.20 ± 0.07	0.25 ± 0.10	1.23 ± 0.07	6.46 ± 0.39	−5.8 ± 2.3 (10.7)
3C58	40.64	0.2163	17.1 ± 0.3	0.99 ± 0.08	0.46 ± 0.09	1.09 ± 0.08	6.37 ± 0.50	−12.6 ± 2.3 (3.9)
3C58	60.52	0.2085	14.1 ± 0.3[d]	0.77 ± 0.12[d]	0.07 ± 0.17[d]	0.77 ± 0.12	5.48 ± 0.87	−2.7 ± 6.3 (13.7)
3C58	92.94	0.1798	11.4 ± 0.6[e]	0.52 ± 0.23[e]	0.42 ± 0.30[e]	0.67 ± 0.26	5.87 ± 2.28	−19.3 ± 11.7 (−2.9)
3C274	22.68	0.2497	21.6 ± 0.6	0.49 ± 0.08	−0.73 ± 0.06	0.88 ± 0.06	4.06 ± 0.31	28.1 ± 2.3 (45.5)
3C274	32.94	0.2041	16.8 ± 0.4	0.43 ± 0.12	−0.69 ± 0.09	0.81 ± 0.10	4.84 ± 0.61	28.9 ± 4.0 (46.3)
3C274	40.61	0.2161	14.3 ± 0.5	0.40 ± 0.14	−0.55 ± 0.10	0.68 ± 0.12	4.72 ± 0.84	26.9 ± 5.5 (44.3)
3C274	60.48	0.2084	10.6 ± 0.3	0.16 ± 0.25	−0.11 ± 0.18	0.20 ± 0.23	1.85 ± 2.15	17.2 ± 29.9 (34.6)
3C274	92.89	0.1800	7.8 ± 0.3	0.41 ± 0.43	−0.43 ± 0.31	0.59 ± 0.37	7.66 ± 4.83	23.0 ± 18.2 (40.4)

Notes.
[a] The second and third columns list effective band center frequency and peak antenna temperature to flux conversion factor Γ, calculated for spectral index values α of −0.72, −1.17, −0.36, −0.42, and −0.73 for Cas A, Cyg A, Tau A, 3C58, and 3C274, respectively.
[b] Polarized flux $P = (Q^2 + U^2)^{1/2}$ with no correction for noise bias.
[c] Polarization position angle is calculated as $\frac{1}{2}\tan^{-1}(-U/Q)$. It is positive for Galactic north through east. The value for equatorial coordinates is given in parentheses. The errors listed are statistical and do not include the potential systematic error of 1.°5 (Page et al. 2003a, 2007).
[d] The uncertainty includes an uncertainty of 0.015 times the flux, to allow for error due to source extent.
[e] The uncertainty includes an uncertainty of 0.037 times the flux, to allow for error due to source extent.

Table 16
Variability Fit Results for Celestial Calibration Sources

Source	K Band[a] (%/yr)	Ka Band[a] (%/yr)	Q Band[a] (%/yr)	V Band[a] (%/yr)	W Band[a] (%/yr)
Cas A	−0.51 ± 0.01	−0.55 ± 0.02	−0.56 ± 0.02	−0.48 ± 0.05	−0.57 ± 0.12
Cyg A	−0.02 ± 0.03	−0.02 ± 0.08	0.02 ± 0.11	0.03 ± 0.32	−0.86 ± 0.93
Tau A	−0.21 ± 0.01	−0.23 ± 0.01	−0.26 ± 0.02	−0.09 ± 0.03	−0.18 ± 0.06
3C58	−0.05 ± 0.09	0.14 ± 0.15	−0.17 ± 0.18	−0.43 ± 0.35	0.47 ± 0.80
3C274	0.22 ± 0.11	−0.19 ± 0.22	0.29 ± 0.29	1.24 ± 0.69	1.28 ± 1.64

Notes. [a] Trends over the seven-year *WMAP* mission, from the linear fits to the fractional variability data shown in Figure 13.

all frequencies. Results are not significantly different if −0.22% per year is used. Table 17 presents parameters from fits to the spectra for *WMAP* data alone and for the combined data. The two fits are generally consistent within their uncertainties over the *WMAP* frequency range. Some notes on the individual sources follow.

Cas A. A slightly curved spectrum gives a better fit to the combined data than a power law (chi-squared per degree of freedom $\chi^2_\nu = 1.20$ compared to $\chi^2_\nu = 2.13$ for a power law). The flattening of the spectrum with increasing frequency was previously noted by Hafez et al. (2008). This may be consistent with observations of spatial variations of the spectrum in Cas A (e.g., Wright et al. 1999, Anderson & Rudnick 1996). Wright et al. (1999) presented spectra of 26 brightness peaks from maps with 7′ resolution at 1.5, 5, 28, and 83 GHz. The data were mostly consistent with power-law spectra, with spectral indices ranging from −0.75 to −0.95. (For comparison, the overall spectral index from a power-law fit to our integrated spectrum from 1.4 to 93 GHz is −0.73). Such a variation will lead to curvature in the integrated spectrum. Wright et al. (1999) also found curvature for some of the brightness peaks with the spectra progressively flattening at the higher frequencies, and noted that such curvature is expected from models of particle acceleration in cosmic ray modified shocks (Reynolds & Ellison 1992).

Within the *WMAP* frequency range, all of the epoch 2000 scaled fluxes are consistent within the uncertainties with the fit to the combined data. This includes the *WMAP* fluxes, the

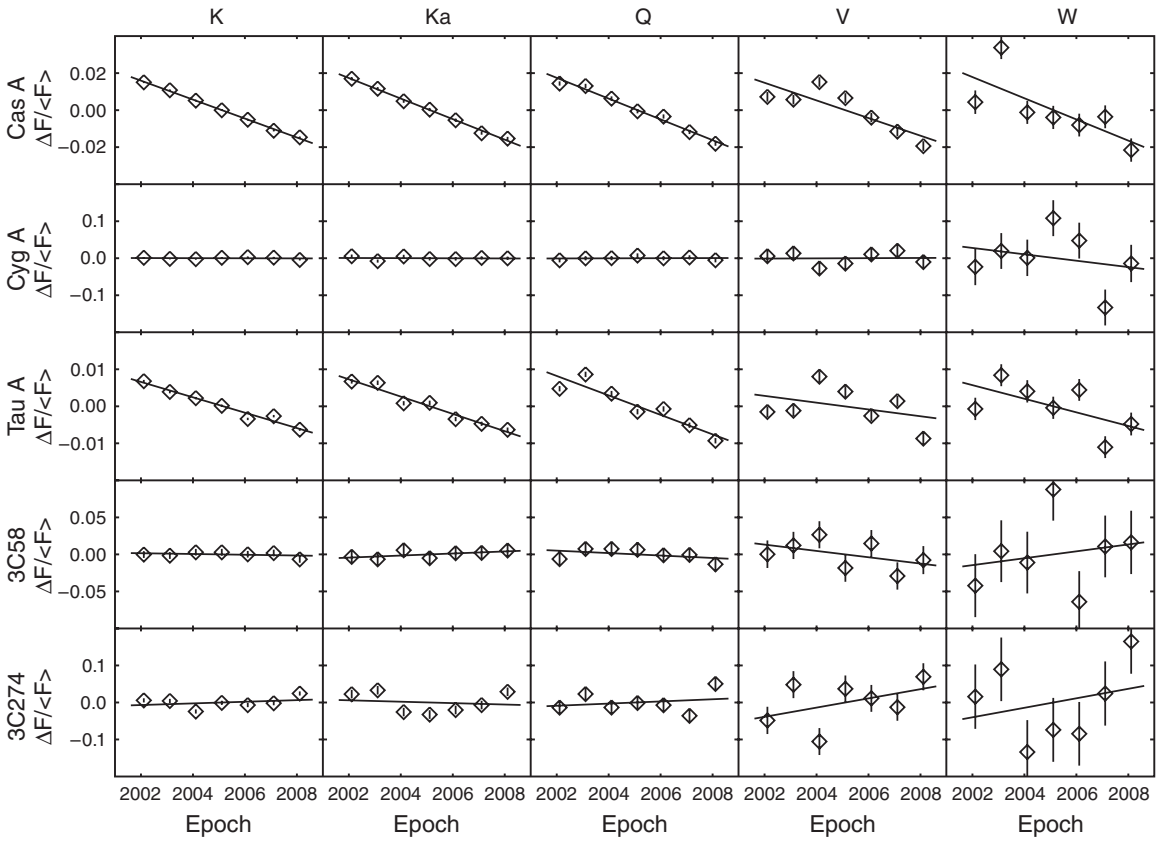

Figure 13. Fractional yearly flux variation measured for the celestial calibrators over the *WMAP* mission. Parameters of the linear fits are listed in Table 16.

Table 17
Spectral Fits for Celestial Calibration Sources

Source	Data	Frequency Range (GHz)	Fit Type[a]	a	b	c	d
Cas A	*WMAP* only	22–93	Power law	2.204 ± 0.002	-0.712 ± 0.018	···	···
Cas A	Combined[b]	1.4–250	Curved	2.204 ± 0.002	-0.682 ± 0.011	0.038 ± 0.008	···
Cyg A	*WMAP* only	22–93	Power law	1.480 ± 0.003	-1.172 ± 0.020	···	···
Cyg A	Combined	2–94	Power law	1.482 ± 0.003	-1.200 ± 0.006	···	···
Tau A	*WMAP* only	22–93	Power law	2.502 ± 0.005	-0.350 ± 0.026	···	···
Tau A	Combined[c]	1–353	Power law	2.506 ± 0.003	-0.302 ± 0.005	···	···
3C58	Combined	0.04–83000	Rolloff	33.7 ± 0.7	-0.053 ± 0.013	0.021 ± 0.006	0.913 ± 0.045
3C274	*WMAP* only	22–93	Power law	1.159 ± 0.005	-0.731 ± 0.030	···	···
3C274	Combined	0.4–93	Curved	1.154 ± 0.005	-0.733 ± 0.013	0.050 ± 0.008	···

Notes.
[a] Power law: log S(Jy) = a + b log (ν/40 GHz), Curved: log S(Jy) = a + b log (ν/40 GHz) +c log^2 (ν/40 GHz), Rolloff: S(Jy) = a (ν/1 GHz)^b/ (1 + c (ν/1 GHz)^d).
[b] The combined data for Cas A were scaled to epoch 2000.
[c] The non-*WMAP* data for Tau A were scaled to epoch 2005.

absolutely calibrated fluxes from Janssen et al. (1974) at 22.29 GHz and Mason et al. (1999) at 32 GHz, the 33 GHz flux from Hafez et al. (2008), which is calibrated using the five-year *WMAP* Jupiter temperature, and the 86 GHz flux from Liszt & Lucas (1999), which is calibrated using the Ulich (1981) Jupiter temperature.

Above 300 GHz, there is excess emission above that expected for synchrotron emission, which has most recently been interpreted as emission from cool dust by Sibthorpe et al. (2010). The 353 and 545 GHz fluxes from Archeops (Desert et al. 2008) are much higher than the 600 GHz flux from BLAST (Sibthorpe et al. 2010) and the 353 and 666 GHz fluxes from SCUBA (Dunne et al. 2003). The Archeops measurements were made with a larger beam ($\sim$12′ compared to $\sim$20″ or better for SCUBA and BLAST) and appear to be affected by dust emission that is not associated with Cas A.

The *WMAP* 23 GHz (*K* band) polarization map for Cas A exhibits unexpected structure. Figure 19 shows seven-year mean intensity and polarization images centered on each source at each of the five *WMAP* frequency bands. These images are $4\overset{\circ}{.}15$ on a side, have not been background subtracted, and are scaled such that brighter pixels are black. The polarization (P) image for Cas A shows an irregular $\sim$0.15 mK ring at a radial distance roughly 40′–50′ from the source position. The angular

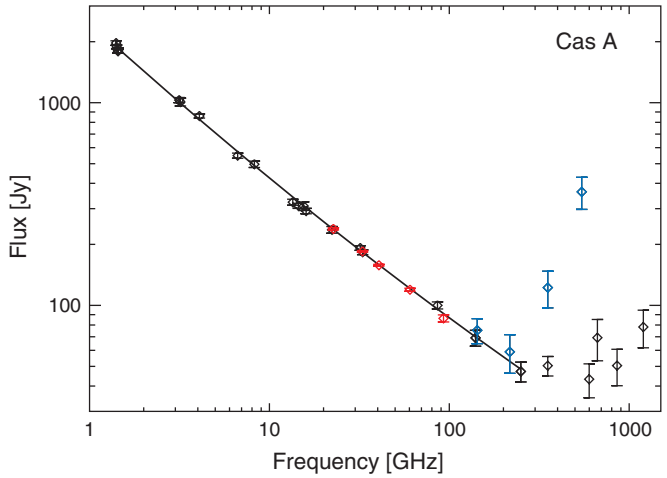

Figure 14. Spectrum of Cas A for epoch 2000. The red symbols show *WMAP* data. The black symbols show data from Hafez et al. (2008), Dunne et al. (2003), and Sibthorpe et al. (2010). The Archeops measurements of Desert et al. (2008), shown in blue, are suspected of being affected by dust emission not associated with Cas A. Black curve is a fit to the combined 1.4–250 GHz data of the form $\log S(\mathrm{Jy}) = a + b \log \nu + c \log^2 \nu$; coefficients are provided in Table 17.

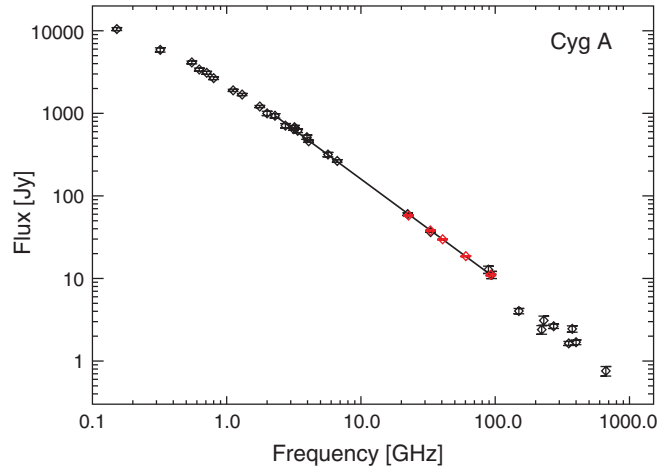

Figure 15. Spectrum of Cyg A. The red symbols show *WMAP* data. The black symbols show data from Baars et al. (1977), Wright & Birkinshaw (1984), Salter et al. (1989b), Eales et al. (1989), Wright & Sault (1993), Robson et al. (1998), and Hafez et al. (2008). Black line is a power-law fit to the combined 2–94 GHz data; coefficients are provided in Table 17.

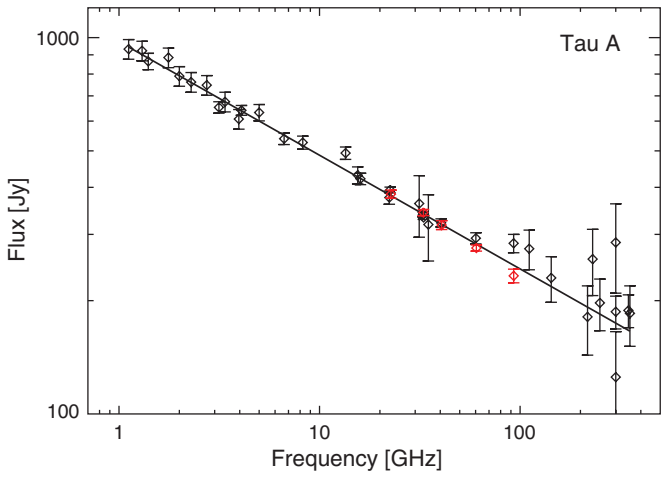

Figure 16. Spectrum of Tau A for epoch 2005. The red symbols show *WMAP* data. The black symbols show data from Macias-Perez et al. (2010) and Hafez et al. (2008). Black line is a power-law fit to the combined 1–353 GHz data; coefficients are provided in Table 17.

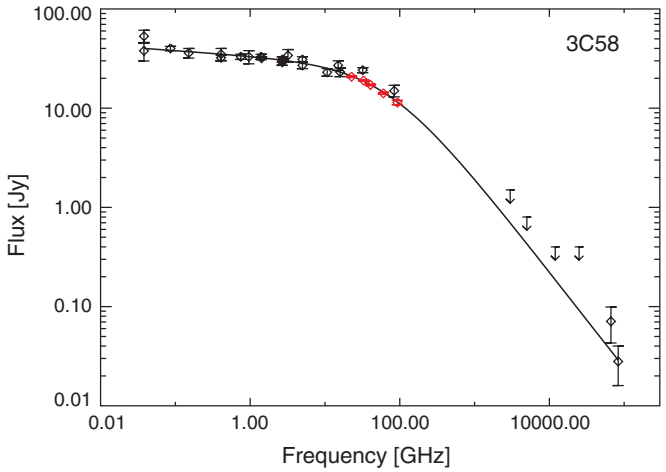

Figure 17. Spectrum of 3C58. The red symbols show *WMAP* data. The black symbols show data from Green (1986), Morsi & Reich (1987), Salter et al. (1989a), Rees (1990), Green & Scheuer (1992), Kothes et al. (2006), Slane et al. (2008), and Hurley-Walker et al. (2009). Black curve is a fit to the combined 0.04–83000 GHz data of the form $S(\mathrm{Jy}) = a\ \nu^b / (1 + c\ \nu^d)$; coefficients are provided in Table 17.

extent of Cas A is $\sim 5'$ (Table 14), leaving the reality of the ring feature in question. We have attempted to simulate this feature under the hypothesis that it is an artifact introduced by a combination of beam and source spectrum characteristics. Cas A is a steep-spectrum source. As a result of effective frequency differences between the two K-band radiometers (Jarosik et al. 2003b), the K11 radiometer (fed by the axial OMT port) has an FWHM roughly 3% wider than that of K12 (which is fed by the lateral OMT port), and the peak observed signal in K11 is a few percent higher than that of K12. Simulated beam maps for the two K-band radiometers were generated separately using Jupiter data as a template, and then individually scaled to peak values representative of Cas A. The difference between the two beams as a function of azimuthal angle and radial distance from beam center can be used to compute a rough estimate of induced Cas A polarization signal, under the assumption of complete scan-angle coverage. Figure 20 shows the results of such a simulation, which produces a feature with an approximately correct peak position (near $50'$), but slightly wider and 30%–40% brighter than that shown in the data image. A more complete simulation would include scan-angle coverage effects, which in this scenario are presumed responsible for the gaps in the ring. This is the only known instance of an apparent artifact in *WMAP* polarization data.

Cyg A. The fluxes from Janssen et al. (1974) at 22.29 GHz, Wright & Birkinshaw (1984) at 89 GHz, and Wright & Sault (1993) at 94 GHz are consistent with the *WMAP* results. The flux from Hafez et al. (2008) at 33 GHz is lower than *WMAP Ka*-band flux by 2.7σ, taking both flux uncertainties into account. We found that excluding the Hafez et al. (2008) flux from the power-law fit to the combined data improved χ^2_ν from 2.89 to 0.79, so it was excluded for the fit plotted in Figure 15 and the fit parameters given in Table 17. Most of the measurements above 100 GHz in Figure 15 are fluxes summed over the core and two hot spots in the radio lobes. These are probably valid measurements of the total flux, since the contribution of extended emission from the steep-spectrum lobes appears to be small or negligible at these frequencies. At 230 GHz, Salter et al.

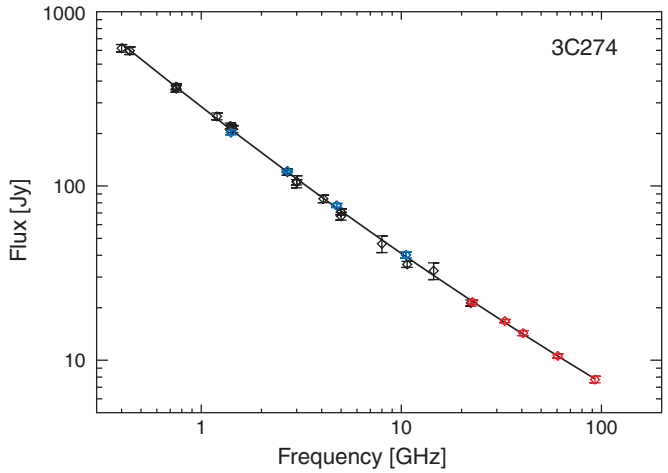

Figure 18. Spectrum of 3C274. The red symbols show *WMAP* data. The black symbols show data from Baars et al. (1977) and blue symbols show data from Ott et al. (1994). Black curve is a fit to the combined 0.4–93 GHz data of the form $\log S(\mathrm{Jy}) = a + b \log \nu + c \log^2 \nu$; coefficients are provided in Table 17.

(1989b) found that the integrated flux over the entire source was only about 10% greater than the summed flux of the hot spots and core, which did not amount to a significant detection of emission from the lobes.

Tau A. The *WMAP* flux agrees with that of Janssen et al. (1974) at 22.29 GHz and with that of Hafez et al. (2008) at 33 GHz. Flux measurements from three-year *WMAP* sky maps by Macias-Perez et al. (2010) are consistent with our results in the K–V bands, but their W-band measurement is 2.8σ greater than ours. The difference is probably due to difference in background subtraction error.

Tau A has been recommended as a polarization calibrator for CMB experiments by Aumont et al. (2010), who report a polarized flux density of 14.5 ± 3.2 Jy at 90 GHz. The *WMAP* value at 93 GHz is 16.6 ± 0.7 Jy. For a 10′ beam, Aumont et al. (2010) predict a position angle of 148.°8 ± 0.°2 (statistical) ±0.°5 (systematic) in equatorial coordinates. The *WMAP* value at 93 GHz is 148.°9 ± 0.°7 (statistical) ±1.°5 (systematic). These measurements and previous position angle measurements integrated over the source are shown as a function of wavelength squared in Figure 21. A linear fit to the data gives an intrinsic polarization position angle of 148.°5 ± 0.°3 and a rotation measure of -24.1 ± 0.2 rad m^{-2}. This mean rotation measure appears to be consistent with the rotation measure map obtained by Bietenholz & Kronberg (1991) from VLA observations at 1.″8 resolution. They found a large-scale rotation measure of ~ -21 rad m^{-2} that they attribute to the interstellar medium, and from the observed depolarization they inferred absolute rotation measure values of a few hundred rad m^{-2} in unresolved filaments.

López-Caniego et al. (2009) report polarized flux densities they measured from 5-year *WMAP* data that are smaller than the values in Table 15 by 9%, 15%, 28%, and 67% at 23, 33, 41, and 61 GHz, respectively. For Cas A, Cyg A, and 3C274, their polarized fluxes agree with those in Table 15 within the uncertainties.

3C58. The *WMAP* data show the spectral steepening first suggested by the 84 GHz measurement of Salter et al. (1989a) and confirmed by the upper limits of Green & Scheuer (1992) in the infrared. Our adopted form for the spectrum transitions between a low-frequency power law and a high-frequency power law, and gives a good fit to the combined radio to infrared data. Our fit gives a change in spectral index of about 0.9. Additional steepening is needed to explain the observed X-ray spectrum, and Slane et al. (2008) suggested there is a second spectral break somewhere in the infrared. They presented model calculations in which the break at ∼100 GHz is due to a break in the electron spectrum injected into the nebula and the higher frequency break is due to synchrotron losses.

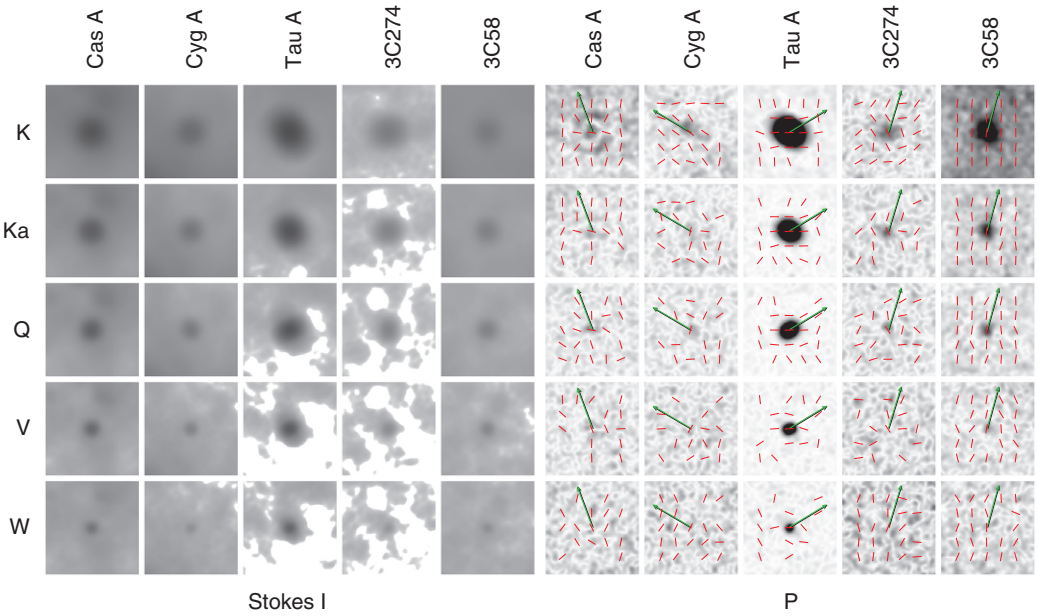

Figure 19. Sky-fixed calibration sources in temperature and in polarization. Each picture is 4.°15 in a side, and the vertical direction is aligned with Galactic north. Sources are labeled along the top, and frequency bands are labeled along the left side. Bright pixels are displayed as black. Left: Stokes *I* logarithmically scaled; peak pixel values in the K band are 60.8, 19.3, 95.8, 5.4, and 7.2 mK thermodynamic, respectively, for the five sources, at a native resolution of HEALPix `nside` = 512. Right: polarization $P = (Q^2 + U^2)^{0.5}$, where Q and U are Stokes parameters, smoothed with a Gaussian of `FWHM` = 13.′5. Scaling is linear between 0 and 0.25 mK thermodynamic, except for Tau A, where scaling is linear between 0 and 1 mK thermodynamic. Green arrow: north in the equatorial coordinate system. Red bars: polarization direction in a square pixel 39′ wide, shown only where the S/N of P is greater than ∼2. The broken ring around Cas A in the K band is spurious and results from beam ellipticity coupled with effective frequency differences between the two orthogonally polarized K-band radiometers.

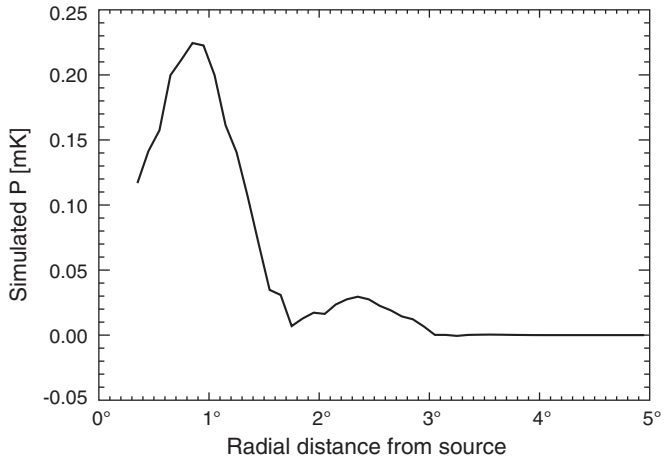

Figure 20. Simplistic simulation of a false polarization signal which would resemble a ring encircling Cas A at a radius of $\sim 50'$. The black line is the radial profile of an azimuthally symmetric polarization artifact centered on the source, resulting from a combination of beam, detector and source properties. The simulation approximately reproduces the observed ring structure surrounding Cas A in Figure 19, but is brighter by $\sim 35\%$, and does not include details such as the asymmetric scan-angle distribution in the data.

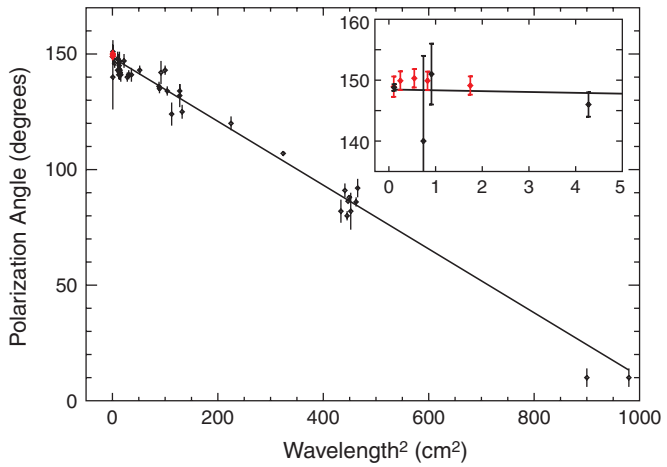

Figure 21. Position angle of integrated polarization of Tau A in equatorial coordinates as a function of wavelength squared. The *WMAP* results from Table 15 are shown in red, with error bars that include a systematic uncertainty of 1.°5. Results shown in black are from references in Wilson (1972) and from Aumont et al. (2010) at 90 GHz for a 10 arcmin beam. The linear fit gives an intrinsic polarization position angle of $148.°5 \pm 0.°3$ and a rotation measure of -24.1 ± 0.2 rad m^{-2}.

3C274. The *WMAP* K-band flux agrees with that of Janssen et al. (1974) at 22.29 GHz. The combined data are better fit by a quadratic ($\chi^2_\nu = 0.99$) than by a linear power law ($\chi^2_\nu = 2.54$). Curvature in the overall spectrum might be expected since 3C274 has a steep spectrum halo. Above 10 GHz, the contribution of the halo to the total flux is <1% (Baars et al. 1977). Over the *WMAP* frequency range, the quadratic fit and the *WMAP* only power-law fit are not significantly different. The data of Ott et al. (1994) give a flatter 1.4–10.6 GHz spectral index than that of Baars et al. (1977), and they suggested that this may be due to core activity that could cause variability at the 5–10% level. As noted above, variability of about 4% and 17% has been observed at 43 GHz and 90 GHz, respectively.

5. CONCLUSIONS

WMAP data provide well-calibrated radiometry of the outer planets and bright sources. The seven-year data provide the longest *WMAP* baseline to date from which to study temporal variability, plus an increase in signal-to-noise which allows us to include fainter objects such as Uranus and Neptune in the analysis.

Jupiter temperatures derived from the seven-year data are within 1σ of the previously published five-year values of Hill et al. (2009). The disk-integrated temperatures derived for Jupiter at *WMAP* frequencies have uncertainties of less than 1%, with an apparent seasonal stability of $\Delta T/T = 0.2\% \pm 0.4\%$. As a planet, Jupiter has additional advantages in that it has a small apparent angular diameter and moves with respect to the fixed sky, allowing for well-characterized background subtraction. Of the ten objects studied, *WMAP* uncertainties for Jupiter are lowest, and we continue to recommend it as the best means for transferring the *WMAP* dipole calibration to another microwave instrument.

With the aid of models to predict geometrical and/or intrinsic variations, the *WMAP*-derived temperatures for Mars and Saturn are predictable to $\leqslant 3\%$. The recommendation for using the Mars values needs to be tempered by the knowledge that these have been derived using mean seasonal properties only. The Saturn model is purely empirical, and can be improved with the addition of the 2009 and 2010 *WMAP* observations when the rings are nearly edge-on.

Uncertainties in the seven-year mean Uranus temperatures range from 3% at the W band to about 7% in the K and Ka bands; only the Q, V, and W measurements are suitable for calibration at the $\lesssim$5% level. Some form of simple model including polar brightness effects would be required to extend the seven-year mean data here beyond the observing epoch, since long-term studies in the literature show clear seasonal temperature variations. There is also the surprising hint of a dip in the microwave spectrum near 30 GHz, where none is expected based on discussions in the literature.

Seven-year mean temperature uncertainties for Neptune exceed 5% at all *WMAP* frequencies and so are not recommended for serious calibration usage.

Flux densities in Stokes *I* for the five celestial calibrators have typical uncertainties of 1%–3%, and are in good agreement with previous measurements in the *WMAP* frequency range. For four of the sources, the *WMAP* data and other available data are consistent with a simple well-defined spectrum over two decades in frequency or more. The *WMAP* observations improve the accuracy of the spectral fit parameters and in some cases they extend the frequency range where the object may be used for calibration. The uncertainties in the spectral fits are typically 1% or less in amplitude and 0.02 or less in spectral index. We provide new estimates for the secular variation of Cas A and Tau A, and provide limits and an estimate for year-to-year variability of the other sources. We present *WMAP* polarization data with uncertainties of a few percent for Tau A.

The seven-year *WMAP* data products are available to the research community through the Legacy Archive for Microwave Background Data Analysis (LAMBDA) at http://lambda.gsfc.nasa.gov.

The *WMAP* mission is made possible by the support of the Science Mission Directorate Office at NASA Headquarters. This research has made use of NASA's Astrophysics Data System Bibliographic Services. We acknowledge the use of the HEALPix package (Gorski et al. 2005).

REFERENCES

Aller, H. D., & Reynolds, S. P. 1985, ApJ, 293, 73
Anderson, M. C., & Rudnick, L. 1996, ApJ, 456, 234
Aumont, J., et al. 2010, A&A, 514, A70
Baars, J. W. M., Genzel, R., Pauliny-Toth, I. I. K., & Witzel, A. 1977, A&A, 61, 99
Bennett, C. L., et al. 2003a, ApJS, 148, 97
Bennett, C. L., et al. 2003b, ApJ, 583, 1
Bennett, C. L., et al. 2011, ApJS, 192, 17
Bietenholz, M. F., Kassim, N., Frail, D. A., Perley, R. A., Erickson, W. C., & Hajian, A. R. 1997, ApJ, 490, 291
Bietenholz, M. F., & Kronberg, P. P. 1991, ApJ, 368, 231
Boggess, N. W., et al. 1992, ApJ, 397, 420
Burgdorf, M. J., et al. 2000, Icarus, 145, 79
Carilli, C. L., & Barthel, P. D. 1996, A&AR, 7, 1
Christensen, P. R. 1998, J. Geophys. Res., 103, 1733
Christensen, P. R., et al. 2001, J. Geophys. Res., 106, 23823
Condon, J. J., Cotton, W. D., Greisen, E. W., Yin, Q. F., Perley, R. A., Taylor, G. B., & Broderick, J. J. 1998, AJ, 115, 1693
Cunningham, C. T., Ade, P. A. R., Robson, E. I., Nolt, I. G., & Radostitz, J. V. 1981, Icarus, 48, 127
de Pater, I. 1990, ARA&A, 28, 347
de Pater, I., & Dickel, J. R. 1991, Icarus, 94, 474
de Pater, I., & Dunn, D. E. 2003, Icarus, 163, 449
de Pater, I., Dunn, D., Romani, P., & Zahnle, K. 2001, Icarus, 149, 66
de Pater, I., Kenderdine, S., & Dickel, J. R. 1982, Icarus, 51, 25
de Pater, I., & Richmond, M. 1989, Icarus, 80, 1
de Pater, I., Romani, P. N., & Atreya, S. K. 1991, Icarus, 91, 220
de Pater, I., et al. 2003, Icarus, 163, 434
Deboer, D. R., & Steffes, P. G. 1996, Icarus, 123, 324
Desert, F.-X., et al. 2008, A&A, 481, 411
Dowling, T. E., Muhleman, D. O., & Berge, G. L. 1987, Icarus, 70, 506
Dunn, D. E., de Pater, I., & Molnar, L. A. 2007, Icarus, 192, 56
Dunn, D. E., de Pater, I., Wright, M., Hogerheijde, M. R., & Molnar, L. A. 2005, AJ, 129, 1109
Dunn, D. E., Molnar, L. A., & Fix, J. D. 2002, Icarus, 160, 132
Dunne, L., Eales, S., Ivison, R., Morgan, H., & Edmunds, M. 2003, Nature, 424, 285
Eales, S. A., Alexander, P., & Duncan, W. D. 1989, MNRAS, 240, 817
Epstein, E. E., Janssen, M. A., Cuzzi, J. N., Fogarty, W. G., & Mottmann, J. 1980, Icarus, 41, 103
Gibson, J., Welch, W. J., & de Pater, I. 2005, Icarus, 173, 439
Gold, B., et al. 2011, ApJS, 192, 15
Goldin, A. B., et al. 1997, ApJ, 488, L161
Gorski, K. M., Hivon, E., Banday, A. J., Wandelt, B. D., Hansen, F. K., Reinecke, M., & Bartlemann, M. 2005, ApJ, 622, 759
Green, D. A. 1986, MNRAS, 218, 533
Green, D. A. 1987, MNRAS, 225, 11P
Green, D. A. 2009, Bull. Astron. Soc. India, 37, 45
Green, D. A., & Scheuer, P. A. G. 1992, MNRAS, 258, 833
Green, D. A., Tuffs, R. J., & Popescu, C. C. 2004, MNRAS, 355, 1315
Greve, A., Steppe, H., Graham, D., & Schalinski, C. J. 1994, A&A, 286, 654
Griffin, M. J., Ade, P. A. R., Orton, G. S., Robson, E. I., Gear, W. K., Nolt, I. G., & Radostitz, J. V. 1986, Icarus, 65, 244
Griffin, M. J., & Orton, G. S. 1993, Icarus, 105, 537
Grossman, A. W., Muhleman, D. O., & Berge, G. L. 1989, Science, 245, 1211
Gulkis, S., Janssen, M. A., & Olsen, E. T. 1978, Icarus, 34, 10
Hafez, Y. A., et al. 2008, MNRAS, 388, 177
Hammel, H. B., & Lockwood, G. W. 2007, Icarus, 186, 291
Harris, D. E., Cheung, C. C., Stawarz, Ł., Biretta, J. A., & Perlman, E. S. 2009, ApJ, 699, 305
Hauser, M., Kelsall, T., Leisawitz, D., & Weiland, J. 1998, COBE Diffuse Infrared Background Experiment (*DIRBE*) Explanatory Supplement, http://lambda.gsfc.nasa.gov/product/cobe/dirbe_exsup.cfm
Hill, R. S., et al. 2009, ApJS, 180, 246
Hinshaw, G., et al. 2003, ApJS, 148, 135
Hinshaw, G., et al. 2007, ApJS, 170, 288
Hinshaw, G., et al. 2009, ApJS, 180, 225
Hofstadter, M. D. 1993, BAAS, 25, 1077
Hofstadter, M. D., & Butler, B. J. 2003, Icarus, 165, 168
Hurley-Walker, N., et al. 2009, MNRAS, 396, 365
Janssen, M. A., Golden, L. M., & Welch, W. J. 1974, A&A, 33, 373
Janssen, M. A., & Olsen, E. T. 1978, Icarus, 33, 263
Jarosik, N., et al. 2003a, ApJS, 145, 413
Jarosik, N., et al. 2003b, ApJS, 148, 29
Jarosik, N., et al. 2007, ApJS, 170, 263
Jarosik, N., et al. 2011, ApJS, 192, 14
Joiner, J., & Steffes, P. G. 1991, J. Geophys. Res., 96, 17463
Junor, W., & Biretta, J. A. 1995, AJ, 109, 500
Klein, M. J., & Gulkis, S. 1978, Icarus, 35, 44
Klein, M. J., & Hofstadter, M. D. 2006, Icarus, 184, 170
Klein, M. J., Janssen, M. A., Gulkis, S., & Olsen, E. T. 1978, in The Saturn System, ed. D. M. Hunten & D. Morrison (NASA Conf. Pub. 2068; Washington, DC: NASA), 195
Kothes, R., et al. 2006, A&A, 457, 1081
Komatsu, E., et al. 2011, ApJS, 192, 18
Kramer, C., Moreno, R., & Greve, A. 2008, A&A, 482, 359
Larson, D., et al. 2011, ApJS, 192, 16
Liszt, H., & Lucas, R. 1999, A&A, 347, 258
López-Caniego, M., Massardi, M., González-Nuevo, J., Lanz, L., Herranz, D., De Zotti, G., Sanz, J. L., & Argüeso, F. 2009, ApJ, 705, 868
Macias-Perez, J. F., Mayet, F., Aumont, J., & Desert, F. X. 2010, ApJ, 711, 417
Marouf, E. A., Tyler, G. L., Zebker, H. A., Simpson, R. A., & Eshleman, V. R. 1983, Icarus, 54, 189
Marten, A., Matthews, H. E., Owen, T., Moreno, R., Hidayat, T., & Biraud, Y. 2005, A&A, 429, 1097
Mason, B. S., Leitch, E. M., Myers, S. T., Cartwright, J. K., & Readhead, A. C. S. 1999, AJ, 118, 2908
Miyoshi, Y., Misawa, H., Morioka, A., Kondo, T., Koyama, Y., & Nakajima, J. 2000, Adv. Space Res., 26, 1533
Morabito, D. D., Preston, R. A., & Jauncey, D. L. 1988, AJ, 95, 1037
Morsi, H. W., & Reich, W. 1987, A&AS, 69, 533
Muhleman, D. O., & Berge, G. L. 1991, Icarus, 92, 263
Orton, G. S., & Burgdorf, M. J. 2003, in The Calibration Legacy of the *ISO* Mission, ed. L. Metcalfe et al. (ESA-SP 481; Noordwijk: ESA), 1470
O'Sullivan, C., & Green, D. A. 1999, MNRAS, 303, 575
Ott, M., Witzel, A., Quirrenbach, A., Krichbaum, T. P., Standke, K. J., Schalinski, C. J., & Hummel, C. A. 1994, A&A, 284, 331
Page, L., et al. 2003a, ApJS, 148, 39
Page, L., et al. 2003b, ApJ, 585, 566
Page, L., et al. 2007, ApJS, 170, 335
Poulet, F., Cruikshank, D. P., Cuzzi, J. N., Roush, T. L., & French, R. G. 2003, A&A, 412, 305
Putzig, N. E., & Mellon, M. T. 2007, Icarus, 191, 68
Rees, N. 1990, MNRAS, 244, 233
Reichart, D. E., & Stephens, A. W. 2000, ApJ, 537, 904
Reynolds, S. P., & Ellison, D. C. 1992, ApJ, 399, L75
Robson, E. I., Leeuw, L. L., Stevens, J. A., & Holland, W. S. 1998, MNRAS, 301, 935
Rudy, D. J., Muhleman, D. O., Berge, G. L., Jakosky, B. M., & Christensen, P. R. 1987, Icarus, 71, 159
Salter, C. J., Reynolds, S. P., Hogg, D. E., Payne, J. M., & Rhodes, P. J. 1989a, ApJ, 338, 171
Salter, C. J., et al. 1989b, A&A, 220, 42
Santos-Costa, D., Bolton, S. J., & Sault, R. J. 2009, A&A, 508, 1001
Schloerb, F. P., Muhleman, D. O., & Berge, G. L. 1980, Icarus, 42, 125
Seidelmann, P. K., et al. 2007, Celestial Mech. Dyn. Astr., 98, 155
Sibthorpe, B., et al. 2010, ApJ, 719, 1553
Sidher, S. D., et al. 2000, Icarus, 147, 35
Slane, P., Helfand, D. J., Reynolds, S. P., Gaensler, B. M., Lemiere, A., & Wang, Z. 2008, ApJ, 676, L33
Smith, M. D., Conrath, B. J., Pearl, J. C., & Christensen, P. R. 2002, Icarus, 157, 259
Spilker, L. J., et al. 2006, Planet Space Sci., 54, 1167
Spilker, T. R. 1995, Earth, Moon and Planets, 67, 89
Tyler, G. L., Marouf, E. A., Simpson, R. A., Zebker, H. A., & Eshleman, V. R. 1983, Icarus, 54, 160
Steppe, H., Salter, C. J., Chini, R., Kreysa, E., Brunswig, W., & Lobato Perez, J. 1988, A&AS, 75, 317
Ulich, B. L. 1981, AJ, 86, 1619
van der Tak, F., de Pater, I., Silva, A., & Millan, R. 1999, Icarus, 142, 125
Verbiscer, A. J., Skrutskie, M. F., & Hamilton, D. P. 2009, Nature, 461, 1098
Vinyaikin, E. N., & Razin, V. A. 1979a, Astron. Zh., 56, 913
Vinyaikin, E. N., & Razin, V. A. 1979b, Aust. J. Phys., 32, 93
Wagner, R. M., et al. 2009, arXiv:0912.3597
Weiland, J., et al. 2011, ApJS, 192, 19
Wilson, A. S. 1972, MNRAS, 157, 229
Wright, E. L. 1976, ApJ, 210, 250
Wright, E. L. 2007, arXiv:astro-ph/0703640
Wright, E. L., & Odenwald, S. 1980, BAAS, 12, 456
Wright, E. L., et al. 2009, ApJS, 180, 283
Wright, M., & Birkinshaw, M. 1984, ApJ, 281, 135
Wright, M. C. H., & Sault, R. J. 1993, ApJ, 402, 546
Wright, M., Dickel, J., Koralesky, B., & Rudnick, L. 1999, ApJ, 518, 284